

https://dspace.org/

Constraining the star formation history with Fermi-LAT observations of the gamma-ray opacity of the universe

Le Ray, Ashlynn Merial

2021
https://hdl.handle.net/10539/32452

Downloaded from a DSpace repository. https://dspace.org/

Constraining the star formation history with Fermi-LAT observations of the gamma-ray opacity of the Universe

Ashlynn Merial Le Ray

Supervisor: Prof. Andrew Chen



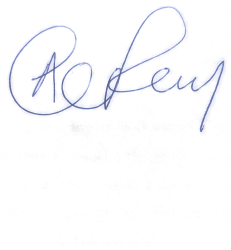
A Dissertation Submitted to the Faculty of Science, University of the Witwatersrand, Johannesburg, in Fulfillment of the Requirements for the Degree of Master of Science.

Johannesburg, South Africa

14, January, 2021

Declaration

I, Ashlynn Merial Le Ray the undersigned, hereby declare that the work contained in this MSc. thesis is my original work and that any work done by others or by myself previously has been acknowledged and referenced accordingly. This thesis is submitted to the School of Physics, Faculty of Sciences, University of the Witwatersrand, Johannesburg, South Africa, in fulfillment of the requirements for the degree of Master of Science in Physics. It has not been submitted before for any degree or examination in any other university.



Ashlynn Merial Le Ray, 14 January 2021

Dedication

I dedicate this dissertation to my mother, Marsha.
It is impossible to thank you adequately for everything
you've done for me. Without you none of this matters.

Acknowledgements

I would like to take this opportunity to thank and express my gratitude to my supervisor, Prof. Andrew Chen. He has inspired me to become an independent researcher and helped me realize the power of critical reasoning. He has been an excellent example of patience throughout this entire journey and allowed me to grow as a researcher. His important suggestions, generosity and advice are priceless. To all my friends in the office who never ceased to encourage and support me throughout this journey. I want thank my sister, Monique for being my rock, my cheerleader and the person who never ceased to remind me why I embarked on this journey. I would like to express my sincere appreciation to the people who patiently helped me with programming, despite their busy schedules. You guys helped make all this possible, thank you. I gratefully appreciate the funding received towards my Masters from the National Research Foundation (NRF). The opacity data used in this work was provided by Fermi-LAT.

CONTENTS

Declaration **1**

Dedication **1**

Acknowledgements **1**

List of Symbols **7**

List of Abbreviations **8**

ABSTRACT 9

I INTRODUCTION **10**

1.1 Background 10
1.2 Problem statement 12
1.3 Aims 12
1.4 Outline of this work 12

II What is the Extragalactic Background light? **13**

2.1 Contributors to the EBL 13
2.1.1 The Hertzprung-Russell diagram 14
2.1.2 The stellar contribution of the EBL 15
2.1.3 Star formation and star formation history 16
2.1.4 Processes of absorption and re-emission that occur in the ISM . . . 18
2.2 Computation of the EBL 19
2.2.1 Models of the EBL 20
2.2.2 The Forward Evolution model 20
2.2.3 The Backward Evolution model 21
2.2.4 The Semi-analytical Models (SAM) 21
2.3 Gamma-ray Astrophysics 23
2.3.1 Gamma-ray Emission mechanisms 24

2.3.2 Sources of gamma-ray emission at GeV-TeV energies 26
2.3.3 Gamma-ray interactions with matter 28
2.4 Gamma-ray Detection 30
2.5 A brief discussion of the Fermi-LAT 31

III Method **32**
3.1 Introduction 32
3.2 SSP Software Models 33
3.2.1 GALAXEV 33
3.3 Individual spectra extraction from GALAXEV and its connection to the computation of the EBL 34
3.3.1 Bruzual & Charlot (2003) 34
3.3.2 Extracting individual spectra 35
3.3.3 Computation of the Extragalactic Background Light (EBL) 35
3.4 Calculation of the Emissivity 35
3.4.1 Spectral Synthesis model 36
3.4.2 Low metallicity SEDs 36
3.4.3 Interstellar medium and dust attenuation 38
3.4.4 Average Dust extinction 38
3.4.5 Re-emission computed as the addition of three modified Blackbody spectra 38
3.4.6 Cosmology 41
3.5 Calculation of the EBL using different parameters of star formation rate . . 44
3.5.1 The Best-fit Model 44
3.6 Gamma-ray attenuation 45

IV Results and discussion **48**
4.1 Topics of the investigation 48
4.1.1 Best fit Star formation rate model and Emissivity 48
4.1.2 The EBL at various redshifts using best-fit model 49
4.1.3 Summary of different models used to calculate the EBL, including the model used in this work 53
4.1.4 Gamma-ray opacity of the Universe 54

V Conclusions **55**

Bibliography **65**

List of Tables

3.1 Dust parameters used in the calculation of the dust spectra of the EBL. . . . 39
3.2 SFH parameters used in the calculation of the of the star formation rate .The values were obtained from (Kneiske et al., 2004). 44

List of figures

2.1 This figure depicts the intensity of the Extragalactic Background Light as a function of wavelength/frequency. The cosmic optical background (COB) and the cosmic infrared background (CIB) are illustrated as 'bumps'. Also shown is the cosmic microwave background (CMB). The numbers indicate total intensity in the bands. Figure adopted from Bavouzet et al. (2008). . . 14
2.2 The Hertzsprung-Russell-diagram. This figure depicts the various stages in the stellar evolution process. From the figure it is evident that the most prominent feature, is the main sequence (grey), which runs from the upper left (hot, luminous stars) to the bottom right (cool, faint stars) of the diagram. The giant branch and supergiant stars lie above the main sequence, and white dwarfs are found below it. Credit:Hollow (2003). 15
2.3 Stellar evolution. Encyclopædia Britannica, Inc. 17
2.4 This figure illustrates the magnificent Orion Nebula. The opulent red glow that percolates the Orion nebula is a result of hydrogen emission. The presence of hydrogen suggests the existence of young hot stars and that processes such as ionization are taking place within the nebula. The specks of blue that are observed at the edges of some of the clouds are a result of scattering. Lastly, irregular contours of dust are also visible intertwined with the glowing gas. Credit: NASA,ESA, M. Robberto (Space Telescope Science Institute/ESA) and the Hubble Space Telescope Orion Treasury Project Team 18

2.5 This figure illustrates the EBL calculated using a forward evolution model: (solid triangles), Davies et al. (1997), (solid violet line) CH, Calzetti and Heckman (1999), (red, green, blue solid lines), depict two possible alternative star formation histories, respectively Dwek (1998). Each given by a sum of two components: the ultraviolet optically determined CSFR and the second is either sharply peaked at z=1.5 and gradually declines at higher redshifts. This figure shows the comparison of the predictions of different FE models and the observed EBL spectrum. The limits from observations are represented by the yellow band. Note: these limits are more than two decades old and are obsolete. There are more recent measurements and limits, those should be used. This figure is adopted from Hauser and Dwek (2001). 19
2.6 The illustration of the Bremsstrahlung interaction discussed in the text is shown in this schematic. From the figure, we see that when a charged particle is deflected by another charge, Bremsstrahlung radiation is emitted. Figure adopted from Chris (2001 (accessed August 24, 2020)) 23
2.7 The Inverse Compton interaction discussed in the text. Figure adopted from Ertley (2014). 26
2.8 Schematic representation of particle and antiparticle annihilation. Credit: University (May 2014 (accessed March, 2020)). 27
2.9 The photoelectric effect in an atom. Credit: Ertley et al. (2012). 28
2.10 This figure is a schematic of a γ-ray space telescope spark chamber where the incoming γ-ray converts into an electron positron pair which is tracked to reconstruct the photon arrival direction while the photon energy is measured within the calorimeter. The anticoincidence is used to reject the particle background. Credit: Thompson (2015). 29

3.1 SSP spectra for various population ages, for a Salpeter IMF, normalized to 1 $M_{\odot}$ is depicted in this figure. The spectral energy distribution (SEDs) of a population of coexistent stars, which is expressed as a function of the age of the population. This was calculated for the following ages: $\tau = 0$, 0.0038, 0.00724, 0.0138, 0.07187,0.28612, 1.434, and 11 Gyrs (from top to bottom, based on calculations by (Bruzual and Charlot, 2003). The figure shows a rapid drop in luminosity as massive stars become supernovae (whose light is not included in these SEDs), and the wave- length of the bulk of the emission shifts to the red as the population ages. 33

3.2 This figure depicts the IR spectra associated with each SSP-spectrum (updated Bruzual and Charlot (2003) stellar populations) shown in Figure 3.1. We assume the dust emits as a combination of three blackbodies, representing three types of dust: a 37 K blackbody representing warm, large dust grains, a 80 K blackbody representing hot, small dust grains, and a 202 K blackbody representing PAHs. Thus, the IR emission is modelled as the sum of three modified blackbody spectra. The details of this calculation are mentioned in Section 3.4.5 37
3.3 This figure depicts the EBL at $z = 0$, calculated using Bruzual and Charlot (2003) stellar population synthesis models at low metallicity ($Z = 0.001$) and best-fit model parameters proposed by Kneiske et al. (2004). The EBL measurements produced in this work agrees with the EBL measurements made by Kneiske et al. (2004) at $z = 0$. These Best-fit model parameters are listed in Table 3.2. 42
3.4 This figure illustrates the reaction of the γ-γ pair and depicts the definition of the angle θ between the interacting photons. Figure adopted from (Dwek and Krennrich, 2013) 45
3.5 The cross section for the γ-γ interaction **Left panel:** The cross section's dependence on β (see Equation 3.19) ; **Right panel:** The cross section's dependence on various incident angles. 46

4.1 This figure illustrates the relationship between the model luminosity density as a function of redshift and a given a star formation rate model. **Left panel:** Total global star formation rate for Kneiske et al. (2004), best-fit model SFR = SFR_{OPT} + SFR_{LIG} ; **Right panel:** The model emissivities are plotted at 1.0 μm, 0.44 μm, 0.28 μm wavelength bands in the optical region from top to bottom. 49
4.2 The comoving-frame EBL using the best-fit model proposed by Kneiske et al. (2004) with updated (Bruzual and Charlot, 2003) models. 50
4.3 This figure illustrates the γ-ray opacity of the Universe at different redshifts, calculated using observed E_γ energies in GeV. The calculations are based on the Kneiske et al. (2004) model. 50
4.4 This figure illustrates the γ-ray opacity of the Universe at different redshifts, where the dashed lines represent the data from Fermi observations Fermi-LAT Collaboration et al. (2018). The solid line shows the predictions of the Kneiske et al. (2004) EBL model. It is apparent from the figure that most of the constraining power is around $\tau_{\gamma\gamma}$ =1 (Tajima, 2013). The value $\tau_{\gamma\gamma}$ = 1 marks the cosmic γ-ray horizon, i.e., the energy above which our Universe becomes opaque to γ-rays for a given redshift. The Fermi data are depicted with error bars. 51

List of Symbols

Ω_m	Matter Density
Ω_Λ	Vacuum Energy Density
$\mathrm{M}_\odot$	Solar Mass
$\mathrm{T}_\odot$	Solar Temperature
$\mathrm{R}_\odot$	Solar Radius
$\mathrm{L}_\odot$	Solar Luminosity
$\mathrm{t}_\odot$	Solar Lifetime
H_0	Hubble Constant
h	Planck's Constant
$\hbar$	Rationalized Planck's Constant
c	Speed of light
e	Elementary Charge of an Electron
m_e	Rest Mass of the Electron
k	Boltzmann's Constant
eV	Electron Volt
I_ν	Spectral Intensity
r_o	Classical Radius

List of Abbreviations

EBL	Extragalactic Background Light
AGN	Active Galactic Nucleus
BE	Backward Evolution
CCE	Cosmic Chemical Evolution
$CSFR$	Cosmic Star-Formation Rate
FE	Forward Evolution Model
ISM	Interstellar Medium
PAH	Polycyclic Aromatic Hydrocarbons
VHE	Very High Energy
IR	Infrared
IMF	Initial Mass Function
LF	Luminosity Function
SAM	Semi-Analytical Model
SED	Spectral Energy Distribution
SFR	Star Formation Rate
$CSFH$	Cosmic Star Formation History
COB	Cosmic Optical Background
CIB	Cosmic Infrared Background
SSP	Simple Stellar Population
SFH	Star Formation History
ΛCDM	ΛCold Dark Matter
$C\Lambda CDM$	'Concordance cosmology' ΛCold Dark Matter
$WMAP$	Wilkinson Microwave Anisotropy Probe 5-year cosmology

ABSTRACT

This work is based on a two-part paper series developed by Kneiske et al. (2002) and Kneiske et al. (2004). Our project investigates the effects of changes in the parameters of star formation history on the predicted extragalactic background light and the gamma-ray opacity of the Universe. We use observations from Fermi-LAT to constrain our model parameters. We introduce a model of stellar emission and dust re-emission as a function of redshift proposed by Kneiske et al. (2002) in our calculations, since the extragalactic background light (EBL) consists of the contribution from dust and stellar emission. The components that contribute to the stellar emission involved the use of simple stellar population (SSP) models that were computed using the Padova (1994) evolutionary tracks Bruzual and Charlot (2003). The SED of an simple stellar population (SSP) is a function of time, since stars progress over various cosmological times, depending on their mass. The infrared emission associated with each SSP-spectrum is computed as the addition of three modified Blackbody spectra. The total spectra of starlight and re-emission are used to calculate the luminosity density, which is then used to calculate the spectrum of the EBL at different redshifts. We use the Best-fit model developed by Kneiske et al. (2004) and updated stellar populations (Bruzual and Charlot, 2003) pertaining to the star formation history (SFH) by constraining the parameters of the SFH which lead to the comoving EBL spectrum. This model leads to EBL predictions to be compared with EBL measurements from Fermi data. We then calculate the optical depth and use Fermi observations to constrain our models. The opacity produced in this work deviates slightly from the observations published by Fermi-LAT.

Chapter I

INTRODUCTION

1.1 Background

When one thinks of the residual light in the Universe as a result of the Big Bang, the cosmic microwave background (CMB) comes to mind, with good reason, as it is the most famous light in the Universe and it provides evidence for the Big Bang theory and the cosmological standard model. However, the focus of this thesis is not the CMB, but rather the residual radiation that exists as a result of star formation over the history of the Universe. Star formation began shortly after the Big Bang 13.7 billion years ago; during this process, the Universe cooled enough to let atoms form, which eventually clumped together to create the first stars Larson and Bromm (2001). The light from these stars has been filling our Universe ever since they ignited, thus creating a ubiquitous radiance that permeates space, to which each successive generation of stars adds. This gleam of light is now known as the extragalactic background light (EBL) or rather the "history book of the Universe" Larson and Bromm (2001), even though the EBL is considered one of the most prominent sources of radiation in the Universe apart from the CMB. It must be mentioned that the CMB and the foreground radiation from the Milky Way are separate entities and are thus not included in the spectrum of the EBL (Yuan et al., 2013; Dwek, 2001; Dwek and Krennrich, 2013). The same holds for both X-rays and γ-rays; even though they are produced by extragalactic sources, they are not considered to be a part of the EBL. The reason for this is directly linked to their diverse production mechanisms: the production of γ-rays and X-rays mostly stem from accretion-powered emission in AGN, whereas the EBL is all the radiation emitted by the stellar component of galaxies. The light contributed from later stars are different from the light contributed from the first stars that ever existed. The stars that were formed when the Universe began are thought to have been different from stars today. They are thought to have been hundreds of times the mass of our sun and their lifetimes were shorter as they may have burned hotter and brighter than stars today. The EBL is the ensemble of photons emitted at all epochs by stars and dust, and provides information about the evolution of galaxies

from very early times up to the present. A vast majority of the EBL energy is found in two wavelength ranges, namely, optical and near-infrared (Franceschini et al., 2008). The optical light consists of direct light from stars, and the infrared light is produced by thermal radiation from dust (Pueschel, 2017).

The EBL is a topic of great interest because it contains an enormous amount of information about the evolution of the universe, giving insight into its structure and astrophysical components. From the above discussion, it is evident that the star formation history (SFH) of the Universe is of fundamental importance to cosmology, not only to galaxy formation itself but also to ongoing efforts to determine cosmological parameters and matter content of the Universe (Razzaque et al., 2009). Star formation processes aid in the understanding of galaxy evolution, making the EBL a powerful tool to probe the star formation history of the Universe. Direct measurements of the EBL pose significant challenges since the observable diffuse radiation consists not only of the radiation of stellar components of galaxies but also the contamination of zodiacal light from our solar system as well as the foreground light from our Galaxy (Costamante, 2013). An alternative is to perform indirect measurements, which can be attained by using γ-ray astrophysics, specifically the attenuation of γ-ray spectra from extragalactic sources, such as quasars. In this process, a γ-ray photon from a distant astrophysical source travelling through the Universe with energy E_γ and an EBL photon of energy E_{EBL} annihilate and create an electron-positron pair. The amount of extragalactic background light in the line of sight can be probed by studying the observed quasar spectra and comparing them to models of spectra that do not take absorption into account (Yuan et al., 2013). Lower limits placed by counting galaxies can be used to fit models of the EBL from observations obtained from satellites like the Hubble and GALEX (Kneiske and Dole, 2010). The interaction between high energy γ-rays emitted from blazars can be used to set a strict upper limit on the opacity of the universe to the TeV photons at an given redshift (Dwek and Krennrich, 2013). The Fermi γ-Ray Space Telescope was launched into low-earth orbit in the summer of 2008 (Atwood et al., 2009). Since Fermi's launch, its Large Area Telescope (LAT) observes the entire sky in high-energy γ-rays every three hours, creating the most detailed map of the Universe ever known at these energies. The Fermi telescope can measure the diffuse background as well as resolve point sources. It is sensitive to photon energies ranging from 20 MeV up to $\sim$100 GeV. Observations of blazars are one of the primary drivers of the Fermi γ-Ray Space Telescope (Franceschini et al., 2008). Blazars are characterized by having a pair of relativistic jets one of which is pointing towards Earth, carrying highly energetic plasma away from the AGN, providing a Doppler boost to the observed gamma-ray flux. A signature of the EBL spectral distribution is expected in the observed very high energy (VHE, 100 GeV) spectra of extragalactic sources (Domínguez et al., 2013). This is due to the properties of the interaction. A γ-ray photon interacts mainly with an EBL photon within a well-defined and narrow wavelength range, extending between 0.1 – 1000 μm, which leaves a visible imprint in the spectra of distant AGN. The Fermi-LAT

instrument builds up an increasingly detailed picture of the γ-ray sky and has observed an extensive sample of AGN extending out to large redshifts ($z < 2.56$) which has been used by the Fermi-LAT collaboration to study the EBL (Ackermann et al., 2012).

1.2 Problem statement

About two decades ago, the derivation of the Extragalactic Background light (EBL) from galaxy observations became a powerful tool. Around this (1998) time spaced-based instruments and large-scale surveys were constructed, which aided in studies of the EBL. In 1998 the Hubble Space Telescope (HST) was used to observe emission and star formation histories within galaxy populations, which Madau et al. (1998) used to predict the EBL. One year later chemical histories observed in Lyman-alpha systems were introduced in the modelling of the background flux, which agreed with background flux levels set by observations Fall and Pei (1999). In 2001 Infrared Space Observatory (ISO) data was used to make IR predictions (Franceschini et al., 2001). In this work, we use updated (Bruzual and Charlot, 2003) stellar population synthesis models to reproduce (Kneiske et al., 2004) EBL with the use of their best-fit model, and compare opacity calculated from this model to Fermi observations (Fermi-LAT Collaboration et al., 2018).

1.3 Aims

This project aims to create models of the SFH and use it to model the EBL, calculate the γ-ray opacity of the Universe and use the Fermi data to constrain our models. We achieve this by using a model of starlight and dust re-emission to model the EBL. Lastly, we use new new measurements of the gamma-ray opacity obtained by the Fermi analysis team.

1.4 Outline of this work

The contents of this dissertation are as follows: Presented in this Chapter is a brief discussion of the relevance and importance of the EBL. The remaining four chapters will be presented as follows: a literature review will be covered in Chapter 2, which will be an in-depth review of the concepts and ideas used in this work. The Methodology used in the modelling of the EBL, modelling of the SFH and the calculation of the γ-ray opacity of the Universe is presented in Chapter 3. An in-depth discussion of our results and our findings will be presented in Chapter 4. Conclusions that can be drawn from our results are discussed in Chapter 5.

Chapter II

What is the Extragalactic Background light?

The Extragalactic Background Light (EBL) is one of the fundamental observational quantities in cosmology (Dwek and Krennrich, 2013). The EBL is the radiation interlaced from resolved and unresolved extra-terrestrial sources. A portion of the EBL is resolved into galaxies that, with the aid of giant telescopes with increasing detecting power and higher sensitivities, are seen to deeper and deeper limiting magnitudes (Mattila and Väisänen, 2019). Thus, this resolved part is now known to contribute a substantial part of the EBL.

The Cosmic Microwave Background (CMB) is a faint cosmic background radiation filling all space that is an important source of data on the early Universe because it is the oldest electromagnetic radiation in the Universe; it arises from the last scattering surface of the expanding universe, before re-ionization.The CMB energy density is considered to be the dominant radiation energy density in the Universe. However, the CMB is a source of radiation that is not related to starlight in galaxies; its contribution to the EBL spectrum will not be considered in this work. Thus, after the cosmic microwave background radiation, the EBL produces the second most energetic diffuse background, making it essential for the understanding of the full energy balance of the Universe.

2.1 Contributors to the EBL

The extragalactic background light (EBL) is composed of photons that were radiated at all eras by stars and dust, thus providing information about the evolution of galaxies from very early times up to the present (Franceschini et al., 2008). A vast majority of the EBL energy is found in two wavelength ranges, namely, optical and near-infrared. The near-infrared radiation is produced by thermal radiation from dust.

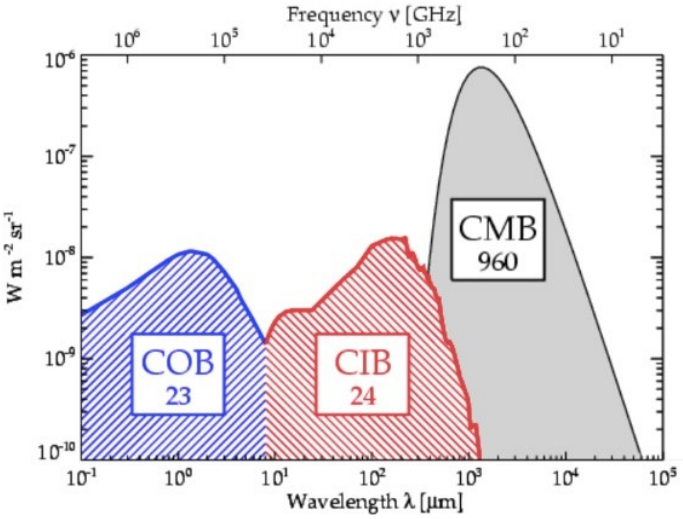


Figure 2.1: This figure depicts the intensity of the Extragalactic Background Light as a function of wavelength/frequency. The cosmic optical background (COB) and the cosmic infrared background (CIB) are illustrated as 'bumps'. Also shown is the cosmic microwave background (CMB). The numbers indicate total intensity in the bands. Figure adopted from Bavouzet et al. (2008).

As discussed in chapter 1, the cosmic optical background (COB) or rather the stellar component of the EBL exists as a result of all the radiation emitted by stars and galaxies, whereas the cosmic infrared background (CIB) is directly related to the re-radiation of light by dust grains (Ackermann et al., 2012). Thus, the two humps in the spectrum represent the COB and the CIB (Ackermann et al., 2012), See Figure 2.1. The EBL designates just one segment of the diffuse photon field present in the Universe. An indirect means of probing the diffuse radiation fields is through $\gamma - \gamma$ absorption of high-energy gamma rays. In this process, a gamma-ray photon from a distant astrophysical source of energy E_γ and an extragalactic background (EBL) photon of energy E_{EBL} annihilate and create an electron-positron pair (Ackermann et al., 2012).

2.1.1 The Hertzprung-Russell diagram

In around 1910, two incredible astronomers named Einar Hertzsprung and Henry Russell worked independently to develop the Hertzsprung-Russell diagram, commonly known as the HR diagram, see Figure 2.2. This diagram was constructed to study the relationship between stars, temperature, luminosity, colour and size.

Ordinary stars like our sun, for instance, lie between the upper-left band to the lower-left band of the H-R diagram and are known as main-sequence stars. All stars spend most their

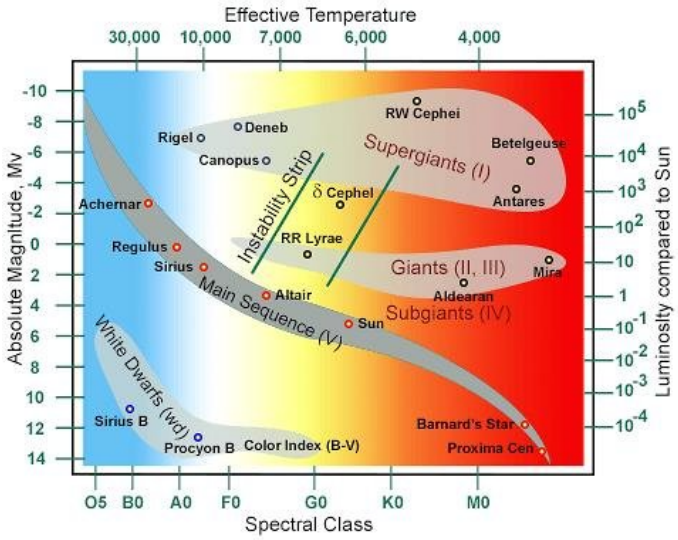


Figure 2.2: The Hertzsprung-Russell-diagram. This figure depicts the various stages in the stellar evolution process. From the figure it is evident that the most prominent feature, is the main sequence (grey), which runs from the upper left (hot, luminous stars) to the bottom right (cool, faint stars) of the diagram. The giant branch and supergiant stars lie above the main sequence, and white dwarfs are found below it. Credit:Hollow (2003).

existence on the main sequence and constitute about 90% of the H-R diagram. The position of main-sequence stars on the H-R diagram ranges from blue stars (which are hotter and larger than small red stars) to cooler red stars. The sun is situated in the middle of the main sequence and is therefore considered to be an average yellow star. It must be noted however that all other (stars other than main sequence) stars are evolved stars which were on the main sequence before.

The upper-right band of the H-R diagram is occupied by a group of luminous stars known as Red giants. These stars are in a late phase of their evolution and their position on the H-R diagram is related to their surface temperatures and intensities. Giants have low surface temperatures and high luminosities which, according to the Stefan-Boltzmann law, means they also have large radii. Stars enter this evolutionary stage once they have exhausted the hydrogen fuel in their cores and have started to burn helium and other heavier elements. Thus, giants are located on the upper right part of the H-R diagram Hollow (2003)

2.1.2 The stellar contribution of the EBL

All the radiation in the Universe that accumulated from star formation processes forms part of the EBL. Radiation emitted from stars with varying metallicities at all redshifts is responsible

for the ultraviolet to the infrared components of the EBL spectrum. Star-forming galaxies are characterized by starburst regions; within these regions abrupt episodes of star formation occur. Speaking of abrupt occurrences of star formation: an assembly of stars produced from synchronic initial conditions namely, time, space and chemical composition are known as Simple Stellar Populations (SSPs) (Kneiske et al., 2002).

An SSP can be described by using four main parameters, namely, its age (t), composition (Y, Z, where Y is the mass fraction of helium, and Z is the mass fraction of all the remaining chemical elements) and the initial mass function (IMF). After a burst of star formation occurs the stellar mass distributed by the burst is governed by a global initial mass function (Orr et al., 2011). The accumulative emission and the duration of the star's existence are mainly determined by its mass and its chemical composition. The abrupt fusion of hydrogen into helium occurring within the cores of massive stars (M > $8M_{\odot}$) lead to a swift stellar lifespan of ($\sim 10^7$ yrs). Massive stars in SSPs produce ultraviolet radiation and have short life spans while low-mass stars have longer life spans and remain within the main sequence over astronomical timescales and are the primary source of the majority of the "red light" (Kneiske et al., 2002). To construct the SED of a single starburst, the age of the population must be considered; thereafter, an integration over the whole stellar population for a given galaxy must be performed. In addition to this, the mass of a star determines the evolutionary path that it will follow. Thus, depending on their mass, stars progress over various cosmological times; for this reason, the SEDs of SSPs become time-dependent. The evolving production of energy is traced using the Bruzual and Charlot (2003) (BC-Model) population synthesis code.

The SEDs presented in this project are constructed from stellar spectra that are based on Padova tracks and Lejeune stellar atmosphere models and a additional post-asymptotic giant branch (post-AGB) evolutionary phase is included (Kneiske et al., 2002). The absorption and re-radiation of starlight by dust and Hydrogen in the interstellar medium (ISM) affects the spectral energy distribution of a galaxy.

2.1.3 Star formation and star formation history

The physical processes that drive star formation are important in the understanding of galaxy evolution. Stars are formed in condensed opaque molecular clouds. The gas within these clouds is cold with temperatures just above absolute zero. Extremely low gas temperatures cause gas to clump together (i.e. causes the gas to become molecular) until the density of the gas reaches a certain threshold, stars form (Kennicutt, 1989). A variety of techniques can be used to estimate current star formation (SF), namely: Hα observations. For example, if one assumes that all photons are absorbed and eventually re-emitted, Hα observations give the number of these ionizing photons, which are almost exclusively emitted by massive (hot)

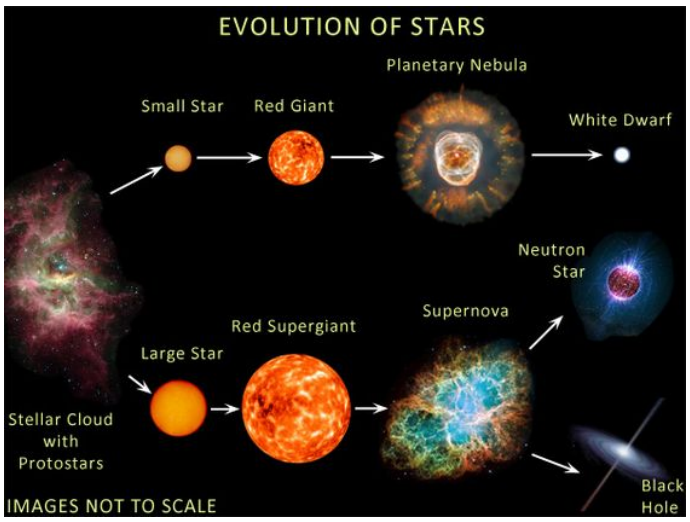


Figure 2.3:
Stellar evolution.
Encyclopædia Britannica, Inc.

stars which have short lifetimes; also the effects of dust can be large and have to be taken into consideration. Another technique uses the far-infrared flux, assuming that a constant fraction of the emitted stellar energy is absorbed by dust. Thirdly, far-UV flux is primarily emitted by young hot stars, and lastly, X-ray emission is produced by 'high mass' X-ray binaries (a neutron star or black hole with a massive companion). Figure 2.3 portrays an elegant depiction of stellar evolution.

The cosmic star formation history (CSFH) is defined as the rate at which stars are born depending upon the age of the Universe. Star formation processes are summed up by the CSFH since the Universe began (Madau and Dickinson, 2014). Massive short-lived stars provide the key to estimating the rate at which stars form. This is achieved through the measurement of UV light that is directly emitted by stars that have a short lifespan. These estimates are found in two wavebands, namely the UV and infrared waveband. The estimates found in the IR are as a result of the re-emission of radiation from dusty star-forming regions. The initial mass function, element enrichment history of the ISM, and the concealment by dust are crucial in understanding the transformation of ultraviolet radiation emitted by stars to stellar mass formed per year (Fermi-LAT Collaboration et al., 2018). The IMF influences most observable properties of stellar populations and thus galaxies, and detecting variations in the IMF could provide deep insights into the star formation process (Kroupa, 2002).



Figure 2.4: This figure illustrates the magnificent Orion Nebula. The opulent red glow that percolates the Orion nebula is a result of hydrogen emission. The presence of hydrogen suggests the existence of young hot stars and that processes such as ionization are taking place within the nebula. The specks of blue that are observed at the edges of some of the clouds are a result of scattering. Lastly, irregular contours of dust are also visible intertwined with the glowing gas. Credit: NASA,ESA, M. Robberto (Space Telescope Science Institute/ESA) and the Hubble Space Telescope Orion Treasury Project Team

.

2.1.4 Processes of absorption and re-emission that occur in the ISM

Interstellar dust grains absorb stellar photons from the ultra-violet to the near-infrared wavelength band, the energy is then re-emitted at longer wavelengths, essentially in the mid and far-IR domains. Dust emission can be split into three broad components, namely, warm dust, cold dust, and polycyclic aromatic hydrocarbons (PAH) components. Emission features around 8 μm are in the mid-IR and are dominated by polycyclic aromatic hydrocarbons (PAH) bands (Kneiske et al., 2002). Warm grains resemble regions heated by the average interstellar radiation field intensities, but progressively become dominated by equilibrium emission at higher intensities. Beyond $\sim$ 100 μm, the emission is increasingly due to big, relatively cold grains (Boquien et al., 2019). The different heating mechanisms of these different dust species, their composition, the metallicity, and the intensity and shape of the incident radiation field, all have an impact on the dust SED (Boquien et al., 2019). The Orion

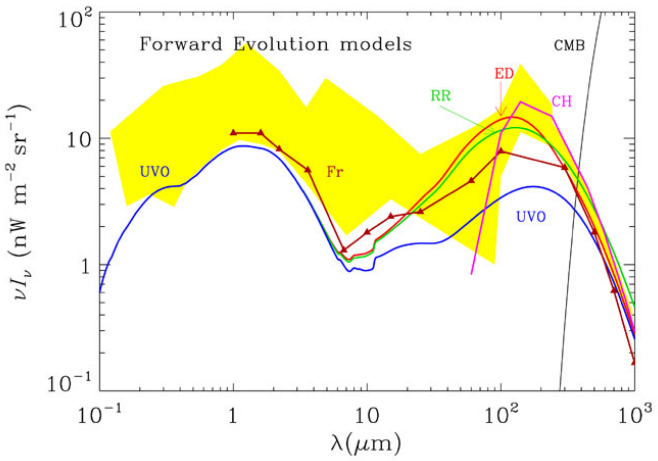


Figure 2.5: This figure illustrates the EBL calculated using a forward evolution model: (solid triangles), Davies et al. (1997), (solid violet line) CH, Calzetti and Heckman (1999), (red, green, blue solid lines), depict two possible alternative star formation histories, respectively Dwek (1998). Each given by a sum of two components: the ultraviolet optically determined CSFR and the second is either sharply peaked at z=1.5 and gradually declines at higher redshifts. This figure shows the comparison of the predictions of different FE models and the observed EBL spectrum. The limits from observations are represented by the yellow band. Note: these limits are more than two decades old and are obsolete. There are more recent measurements and limits, those should be used. This figure is adopted from Hauser and Dwek (2001).

Nebula, an example of a stellar nursery, is shown in Figure 2.4.

It is evident from observations that even the slightest amount of dust can have a substantial effect on the brightness of a galaxy in the mid-IR and far-IR range. The result is an increase in the IR brightness of the galaxy and has been found to exceed the brightness in the optical and near-IR range (Kashlinsky, 2005). Furthermore, if the environment is conducive, the prevalent emission in starburst regions will be attributed to the re-radiation from dust (Kashlinsky, 2005).

2.2 Computation of the EBL

In the following section I will discuss the various models used for the computation of the EBL, the physics involved in these computations as well as their limitations.

2.2.1 Models of the EBL

The estimation of the spectral energy distribution of the EBL requires a variety of factors, which include cosmic evolution of the stellar IMF, CSFR, the evolution of gas metallicity, the radiation emitted by AGN, and gravitational as well as nuclear processes (Dwek, 2001). However, in a dusty Universe, processes like absorption and re-emission cause the energy to be redistributed across the entire spectrum, leaving the EBL intensity unchanged.
The formulation of different EBL models, as well as the deviation from the overall local EBL spectrum, stems from our current understanding of galaxy evolution, SFR processes, and observational limitations. The approach used to determine the comoving luminosity density as a function of redshift (L(z)) separates these models from each other. The strategies adopted by each model can be classified into four groups. Sections 2.2.2, 2.2.3 and 2.2.4 are devoted to the description and discussion of the Forward Evolution model (FE), Backward Evolution model (BE), and the Semi-analytical model (SAM).

2.2.2 The Forward Evolution model

The Forward evolution model begins with cosmological initial conditions (ensuring that the initial conditions satisfy observational data) and follows galaxy evolution forward in time (e.g. Dwek (1998); Razzaque et al. (2009); Finke et al. (2010)). FE models rely on the CSFR as a function of redshift over which the stellar populations are integrated for the formulation of the luminosity density $L_\nu(\lambda, z)$. Figure 2.5 presents the CIB predictions of selected forward evolution models. The solid triangles represent the model of Franceschini et al. (1994). The red, green and blue lines show the models of Dwek (1998) for three distinct cosmic star formation histories. The red line represents a cosmic star formation rate constructed to fit the EBL intensities detected by Cosmic Background Explorer (COBE). The green line represents a cosmic star formation rate with an excess of sources at high redshifts. In this work we use the forward evolution model for the calculation of the EBL. However,the determination of the CSFR becomes difficult as one would have to consider the effects of scattering on the dust, the amount of UV radiation that would be absorbed and lastly the thermal re-emission of infrared radiation. To convert the CSFR to bolometric luminosity requires knowledge of the IMF. Nonetheless, this poses a problem at high redshifts as the parameters are not well understood. After the CSFR is found, the convolution of models of the SEDs of stellar populations (i.e. Leitherer et al. (1999); Fioc and Rocca-Volmerange (1997); Bruzual and Charlot (2003); Orr et al. (2011)) is used to evaluate how the spectral luminosity density changes as a function of redshift (see Chapter 3 for the details of star formation history used in this work).

Radiative transfer models can be used in the determination of the spectral energy distribution of a galaxy (Gordon et al. (2001) & Silva et al. (1998)), as an alternative by using a statistical approach, which involves the absorption of UV light and re-emission of radiation

by dust, which must agree with observations. Radiative transfer models in conjunction with population synthesis models can provide a useful tool in obtaining the UV-radio SED of a given galaxy. Hence, the FE model has been proven to successfully reproduce the global characteristics of the EBL as well as the SED of individual galaxies. There are limitations to using these models, for example, galaxy interactions that are associated with fluctuations in the rate at which stars form are not considered.

2.2.3 The Backward Evolution model

These models begin with existing galaxy populations and extrapolate them backwards in time. The calculation of the luminosity density using the BE model involves the SEDs of diverse galaxies and a luminosity function. In this approach, the Luminosity function is convolved with the SEDs of galaxies. The method entails the determination of the luminosity at redshift zero through extrapolation: this is achieved by using low-redshift observations of galaxy luminosity functions and the extrapolation of those LFs at higher-redshifts (Carroll and Ostlie, 2006). Observations of sources of which the redshift and number counts are known can be used to determine the LF evolution (Dunne et al., 2000) or by using an estimated functional form of the evolution of LF with redshift (Stecker et al., 2006).

The BE model is useful because it allows for the integration of the predicted properties of galaxies and observations. These properties include colour-magnitude and number-magnitude. The Backward evolution model (BE) is solely phenomenological and has no physical processes, meaning that processes that normally govern galaxy evolution (i.e. star formation or radio transfer processes), which are involved in constraining the EBL intensity, are not considered (Dwek and Krennrich, 2013).

2.2.4 The Semi-analytical Models (SAM)

Forward evolution models are extremely useful; however, they are also flawed, especially when it comes to resolving issues pertaining to structural evolution utilised to predict observational properties of galaxies as well as the spectral properties of the EBL. The EBL, including the emergence of galaxies and galaxy clusters in a pyramidal sequence of events of galaxy formation gives a more detailed explanation Cole et al. (2001). Semi-analytical models must consider a number of physical processes, such as the temperature reduction of gas that descends onto dark matter halos, a regulation for star formation, a technique for assessing the efficacy of how stars form, an initial distribution of masses for a population of stars, the efficacy of star formation that occurs during the composition of events, to reproduce observable galaxy properties.

Semi-Analytical models are complex and computationally expensive. The models contain many parameters which can be changed to mirror the properties observed in galaxies in

the Universe at redshift zero (Cole et al., 1994). The modelling of the physical processes involved in SA models is quite cumbersome as some of these physical processes used to derive galaxy properties are poorly understood. The use of SA models is rewarding since they have reproduced several properties observed in galaxies. Quantities of absorption and re-emission must be accurately determined in both models. Despite these difficulties, SA models provide an adequate foundation for the computation of the EBL, which simply put, involves the integration of the radiation over all the modelled galaxies. The same difficulties that are encountered in other EBL models affect SA models as well, including the complications caused by extinction effects in the reproduction of galaxies SED. One should proceed with caution when using both models as they require an accurate determination of the quantities of starlight absorbed and re-emission of radiation by dust. Despite these difficulties, SA models provide a strong foundation for calculation of the extragalactic background light, which in this case, would involve the integration of the light from modelled galaxies, by definition.

The latest pioneering work done by Gilmore et al. (2012) presents a new semi-analytic model that is based on galaxy formation in a Five-year Wilkinson Microwave Anisotropy Probe (WMAP5) cosmology. Gilmore et al. (2012) assumes a standard ΛCDM universe and a Chabrier (Chabrier 2003) stellar initial mass function (IMF) that does not evolve in redshift. Their SAMs are based on Monte Carlo realizations of a dark matter halo (a hypothetical region that has decoupled from cosmic expansion and contains gravitationally bound matter) merger histories. Their work differs from the model developed by Kneiske et al. (2002), which calculates the EBL from the UV-far-IR using 'semi-empirical' method based on measured star formation rates and spectral synthesis models. Starlight is processed by dust, which is modeled as a blackbody with three temperature components. The metallicity is assumed to increase slowly over cosmic time and an average global extinction curve applied to starlight. A follow-up paper, Kneiske et al. (2004), expanded this earlier model into 6 realizations, varying in gas temperature contribution, star formation rate, and UV escape fraction. Kneiske's results are based upon a broken power-law for the star-formation history, with a peak at z=1.2. The history predicted by this SAM model is considerably lower in this epoch, and does not peak until $z \approx 3$ for this SAM CΛCDM model, or $z \approx 2.5$ for the WMAP5 model. Thus, leading to these models having a lower present-day flux, but higher flux at the location of Kneiske's peak and at higher redshifts

Gilmore et al. (2012) uses templates to describe re-emission by dust at mid- and far-IR wavelengths, which is relevant to the interpretation of multi-TeV data from nearby blazars, this is one of the significant weaknesses of their approach. The methodology used in this approach assumes that galaxies of a given bolometric luminosity emit light with a similar spectral distribution. Gilmore et al. (2012)'s Fiducial model does predict slightly higher opacities at high redshift compared to the fiducial model of Gilmore et al. (2009); this is due

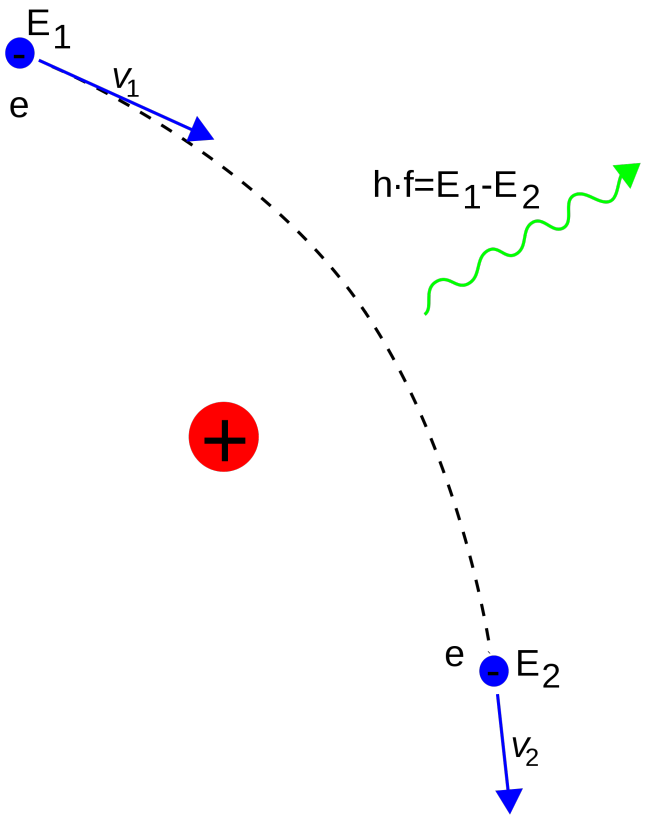


Figure 2.6: The illustration of the Bremsstrahlung interaction discussed in the text is shown in this schematic. From the figure, we see that when a charged particle is deflected by another charge, Bremsstrahlung radiation is emitted. Figure adopted from Chris (2001 (accessed August 24, 2020)) .

to more UV light escaping high-redshift galaxies in our evolving dust model than in the fixed dust model used in the CΛCDM prediction. See Gilmore et al. (2012) for a more detailed discussion.

2.3 Gamma-ray Astrophysics

Gamma radiation is the shortest wavelength electromagnetic wave and imparts the highest photon energy (i.e. photon energies that exceed 100 keV). The last sections of this chapter contain discussions of various γ-ray emission processes, astronomical sources and how γ-rays interact with matter and electromagnetic radiation. The interaction of γ-rays; with the electromagnetic spectrum will be discussed in the methodology section in Chapter 3, specifically in Section 3.6.

2.3.1 Gamma-ray Emission mechanisms

Gamma-rays are produced by non-thermal emission processes. Thermal emission can be modelled as a blackbody, which absorbs all radiation falling on it, reflecting or transmitting none. According to Wien's Law, γ-rays that have energies in the MeV range which require a temperature of the order of 10^{10} K to be emitted. However, temperatures of that magnitude are unattainable in our Universe. The manner in which charge particles interact with electric and magnetic fields are generally known as non-thermal processes, which generate very high energy γ-rays.

Synchrotron and Bremsstrahlung Radiation

Synchrotron radiation is a well-studied phenomenon in electrodynamics. It is the electromagnetic energy emitted by charged particles (i.e. electrons and ions) that are moving at speeds close to the speed of light when their paths are altered by a magnetic field. Mass, momentum, the charge of the accelerated particle, as well as the orientation of the field strength lead to the derivation of the angular distribution, the energy of the spectrum and the quantity of energy radiated by this interaction (Jackson, 1999).

Synchrotron radiation is a free-free emission, which takes place when a charged particle is accelerated by an electric or a magnetic field. The energy of the emitted photon due to the interaction between a cosmic ray with energy (E_e) and the interstellar magnetic field (B) lead to the emission of a photon with energy is given by Equation 2.1, where μG = 10^{-6} Gauss Diehl (2001). Note, this equation is only for electrons.

$$E_\gamma \simeq 0.05 \times \left(\frac{E_e}{(\mathrm{TeV})}\right)^2 \times \frac{B}{3\mu\mathrm{G}}(\mathrm{eV})\,. \tag{2.1}$$

Bremsstrahlung is a German term that means "braking radiation." It is an important phenomenon in the generation of X-rays. To understand this process completely, we require a quantum treatment. This is related to the energy of the photons produced, which is comparable to that of the emitting particle. However, in certain regimes, a classical treatment can be justified and most of the physical parameters have the correct functional dependencies. The quantum results can be stated as corrections (Gaunt factors) to the classical formulas (Rybicki and Lightman, 2008).

The process of free electrons decelerating in the Coulomb field of atomic nuclei and radiating energy is called free-free emission (see Figure 2.6). The term free-free arises from the fact that the radiation is produced by free electrons scattering off ions without being captured—the electrons are free before the interaction and remain free afterwards. More explicitly, during these collisions, electrons move at a velocity with respect to the ions and get

deflected. The electron decelerates and emits a photon due to the electrostatic interaction, bringing away some of its kinetic energy. Hydrogen II (HII) regions are mainly composed of clouds of ionized hydrogen (that is, protons and electrons). An astrophysical example would be HII regions at an equilibrium temperature of 10^4 K (Rybicki and Lightman, 2008).

The energy of the emitted photon E_γ is given in Equation 2.2, Diehl (2001). Note that this equation represents the maximum energy of a photon. The photons can have lower energies.

$$E_\gamma = (\gamma - 1)m_e c^2 \, . \tag{2.2}$$

where $\gamma = \left(\sqrt{1 - \frac{v^2}{c^2}}\right)^{-1}$ is the electron's Lorentz factor. An electron transfers most of its kinetic energy to the Bremsstrahlung photon, leading to the flatness and sharp drop of the braking radiation spectrum. It drops sharply towards zero above, as effectively all the kinetic energy of the electron has been transferred to the bremsstrahlung photon (Diehl, 2001).

The total emissivity, which we obtain by integrating over velocity (energy) distribution

$$\varepsilon_{br}(\nu, T) = 6.8 \times 10^{-38} T^{-\frac{1}{2}} e^{-\frac{h\nu}{kT}} n_e n_z Z^2 g_{ff}(\nu, T) \text{ erg s}^{-1}\text{cm}^{-3}\text{Hz}^{-1} \, . \tag{2.3}$$

where $e^{-\frac{h\nu}{kT}}$ is the high energy cut-off, a cloud with ions is given by number density, n_z and free electron is given by number density, n_e, $g_{ff}(\nu, T)$ is the average gaunt factor, Z is atomic number of hydrogen, h is Planck's constant, ν the frequency of the emitted radiation, T is the temperature of the plasma and k is the Boltzmann constant. For a more detailed overview see Rybicki and Lightman (2008).

Inverse Compton Scattering

The collision between an energetic electron and a low-energy photon can also produce γ-rays. The scattering of low-energy photons to high energies by ultra-relativistic electrons so that the photons gain, and the electrons lose energy is known as Inverse Compton scattering (see Figure 2.7). This process is called inverse because the electrons lose energy rather than the photons, which is the opposite of the standard Compton effect. The energy of the emitted photon from the Inverse Compton effect interaction is (Diehl, 2001):

$$E_\gamma \simeq 1.3 \left(\frac{E_e}{\text{TeV}}\right)^2 \left(\frac{\epsilon}{2 \times 10^{-4} \text{ eV}}\right) \text{GeV} \, . \tag{2.4}$$

where the energy of the electron is given by E_e and the energy of the photon before scattering occurs is given by ϵ.

Nuclear Transitions

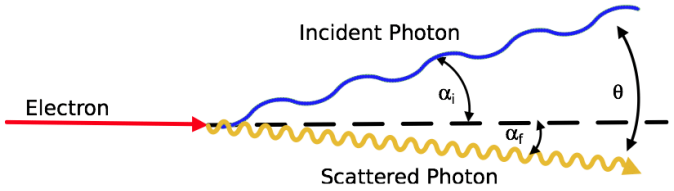


Figure 2.7: The Inverse Compton interaction discussed in the text. Figure adopted from Ertley (2014).

Transitions that occur between energy levels in the nucleus are called nuclear transitions. They lead to the emission of alpha, beta, or gamma radiation. The energy range governed by nuclear transitions are within the MeV regime, hence the transition between different nuclear states requires that the photons involved in absorption or emission are within the MeV regime.

Pion Decay

Neutral and charged pions are produced by the interactions produced by collisions between cosmic rays (protons) and the nuclei of ambient gases. However, the unstable nature of neutral pions (π^0) propels their decay into pairs of γ-ray photons (Schönfelder, 2001).

The decay is given by:

$$\pi^0 \rightarrow \gamma + \gamma \tag{2.5}$$

Annihilation

Annihilation occurs when a particle and an antiparticle collide and disappear, releasing energy. This energy is in the form of a pair of γ-ray photons. Figure 2.8 illustrates the electron-positron annihilation. An electron has a mass of 511 keV which causes the electron-positron annihilation event to occur in the γ-ray range.

2.3.2 Sources of gamma-ray emission at GeV-TeV energies

Sources of γ-rays in the GeV-TeV energy range may be galactic or extragalactic. Extragalactic sources exist outside of the Milky Way whereas Galactic sources are inside the Milky Way galaxy and can, therefore, be less luminous. Galactic sources are characterized according to the mass of original stars, meaning they can be supernova remnants, black holes, diffuse emission, novae, and the Sun. Galactic supernova remnants are among the brightest radio

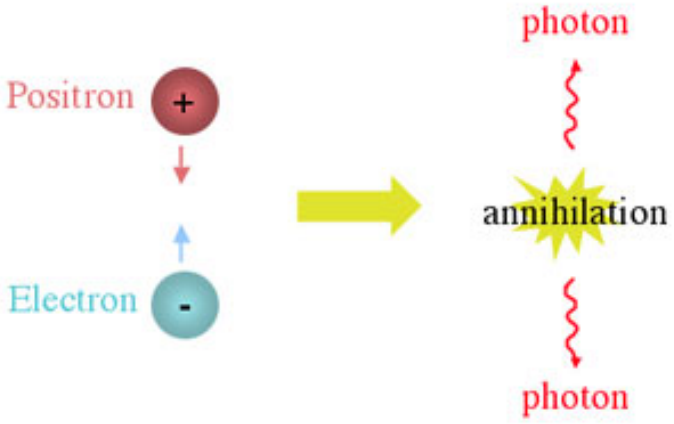


Figure 2.8: Schematic representation of particle and antiparticle annihilation. Credit: University (May 2014 (accessed March, 2020)).

sources on the sky. The emission is synchrotron radiation produced by relativistic electrons that are accelerated in the hot interaction region Branch (2003). Continuum diffuse γ-ray emission is produced in our Galaxy by interactions of high-energy cosmic rays with interstellar matter and low-energy radiation fields. A weaker diffuse component is observed with almost isotropic distribution over the sky, and thus is thought to be extragalactic in origin. This emission is usually referred to as the extragalactic γ-ray background (EGB). The great majority of the EGB can be attributed to unresolved populations of extragalactic gamma-ray sources, primarily the nuclei of active galaxies called blazars Neronov and Semikoz (2020).

A pulsar is a highly magnetized rotating compact star that emits beams of electromagnetic radiation out of its magnetic poles. Pulsars are a source of very high energy (VHE) γ-rays (VHE; $E \gtrsim 100$ GeV). In rotation-powered pulsars, the beam originates from the rotational energy of the neutron star, which generates an electric field from the movement of the very strong magnetic field. High-powered electric fields accelerate charged particles and produce VHE γ-rays. Another source of VHE γ-rays is Inverse Compton scattering. This process involves the scattering of low energy photons to much higher energies, and can occur on the surface of neutron stars (Schönfelder, 2001; Ruderman and Sutherland, 1975).

There are currently several classes of detected γ-ray extragalactic sources, some of which are associated with active galactic nuclei (AGN) and (at soft γ-rays) to γ-ray bursts (GRB) (Bosch-Ramon, 2011). However, it must be noted that there are other extragalactic γ-ray sources such as star-forming galaxies, galaxy clusters, etc. which are not AGN.
There are two types of GRBs, can be long- and short- duration, the first of which may have originated from hypernova or supernova explosions originated from super or hypernova ex-

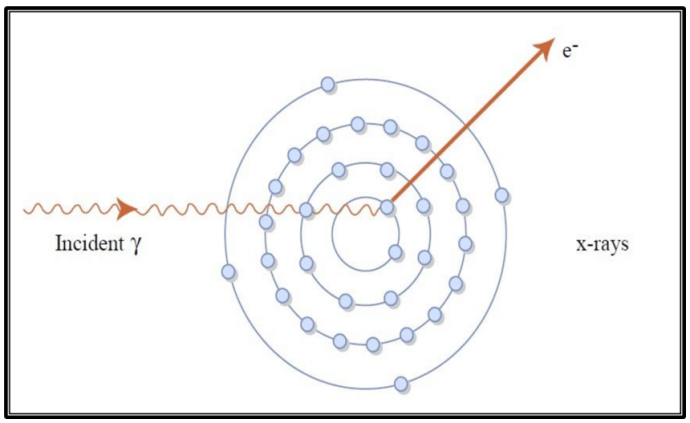


Figure 2.9: The photoelectric effect in an atom. Credit: Ertley et al. (2012).

plosions, and merging neutron stars contribute to the second type of GRBs, respectively. Active galactic nuclei are accreting supermassive black holes hosted by a galaxy that present in some cases powerful relativistic jet activity (Blandford et al., 2019). These sources are probably the most energetic astrophysical objects and have been studied in gamma-rays for several decades. Their appearance depends much on whether their jets point to us (Blandford et al., 2019).

2.3.3 Gamma-ray interactions with matter

The photoelectric effect is a phenomenon in which an electron is released from an atom when it absorbs electromagnetic radiation. In this particular scenario the electrons are in a metal and are not bound to an individual atom. The energy absorbed by the photon can lead to many different scenarios (i.e. the excitation of an electron into orbit, if the photon has enough energy). Figure 2.9 portrays the photoelectric effect in an atom. This interaction favours photons in the 100 eV to 100 keV range (low energy photons).

Compton scattering

This effect involves the scattering of a photon by a charged particle, usually an electron. Compton scattering is the interaction between a high-energy photon and a low-energy or stationary charged particle, usually an electron. It results in an increase in wavelength and thus a decrease in the energy of the photon. The photon may be an X-ray or gamma-ray. Some of the energy of the photon is transferred to the recoiling electron. This differs from the Inverse Compton effect, which occurs when a charged particle transfers some of its energy to a photon. These interactions occur within 100 eV-MeV energy range.

Pair Production

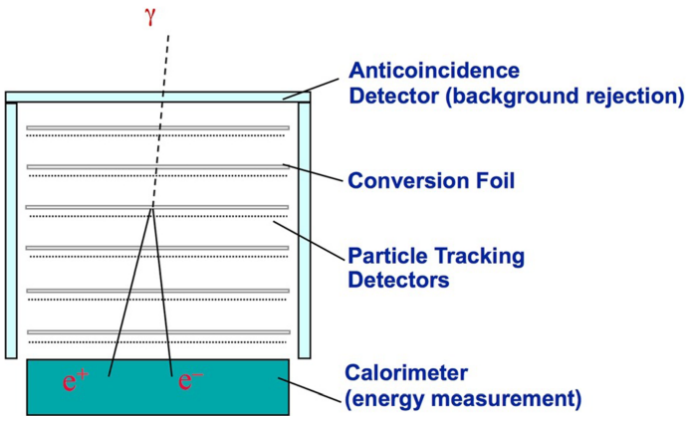


Figure 2.10: This figure is a schematic of a γ-ray space telescope spark chamber where the incoming γ-ray converts into an electron positron pair which is tracked to reconstruct the photon arrival direction while the photon energy is measured within the calorimeter. The anticoincidence is used to reject the particle background. Credit: Thompson (2015).

Pair production is the creation of a subatomic particle and its antiparticle. However, pair production only occurs for γ-rays of high energy. An electron has a rest mass equivalent to 0.511 MeV of energy; therefore, a minimum γ-energy of 1.02 MeV is required for pair production. The presence of a strong electric field is required for this interaction.

Pair production also can occur in the field of an atomic electron, to which considerable recoil energy is thereby imparted. The threshold for such a process is four times the rest energy of an electron, or $4mc^2$ The total pair-production cross section is the sum of the two components, nuclear and electronic. These cross sections depend on the energy of the γ-ray and are usually calculated in an electron theory proposed by the British physicist P.A.M. Dirac through a method of approximation that is a simplification of a method (a "first approximation") devised by the German physicist Max Born Burton (2017 (accessed August 20, 2020)).

How to Detect High-Energy Gamma Rays?

γ-rays, at least at energies above 10's of MeV, interact by electron-positron pair production (E=mc^2); a γ-ray telescope is really a particle detector. This same interaction process makes the Earth's atmosphere opaque to these γ-rays see Figure 2.10.

Electromagnetic cascades

In particle physics, a cascade of secondary particles can be produced as the result of high-energy particles interacting with dense matter. The incoming particle interacts with atoms in

the material in producing several new particles with lesser energy; each of these will continue creating many thousands, millions of new interaction until all the energy has been absorbed.

2.4 Gamma-ray Detection

γ-ray observations are associated with several challenges; for instance, the probability of gamma-rays with energy of 1 MeV being absorbed by our atmosphere is 99.8% (i.e. they interact with atoms in the atmosphere and can produce ions by dislodging electrons from the atoms). This implies that our atmosphere is optically thick, making it impossible to observe γ-rays directly from the earth's surface. The number of γ-ray photons is smaller than the number of optical photons, meaning that the cosmic γ-ray flux is significantly smaller than the optical flux. The difference in flux is due to the energy content of each photon; γ-rays carry more than one million times more energy than optical photons, and this therefore makes it more difficult to produce γ-rays in the first place (Schönfelder, 2001). γ-rays can be detected using two different approaches. The use of space telescopes is one approach, which investigates the interactions of γ-rays with matter, discussed in Section 2.3.3.

Another approach involves the use of ground-based telescopes: this method takes advantage of the effects of the interaction of γ-rays with the atmosphere and does not detect γ-ray emission directly. Optical telescopes are used to detect the Cherenkov radiation resulting from the electromagnetic cascades produced in the atmosphere.

How is the EBL determined from GeV/TeV sources?

The answer to this question can be resolved by looking at the high-energy spectra produced by GeV/TeV sources. In particular, the observed spectra can be compared to models of the intrinsic spectra to measure the EBL from γ-ray observations.

The EBL can be constrained using different sources, such as blazars. Blazars make up most of the extragalactic sources emitting very high energy gamma-rays and are therefore used in current studies to provide constraints on the UV-IR emission of the EBL. Most of the VHE source spectra follow a power-law of the form $\frac{dN}{dE} \propto E^{-\Gamma}$ over a wide energy range. Upon analysis of blazars, a sharp cut-off is detected between GeV and TeV energy ranges. This change is defined as $\triangle\, \Gamma_{GeV} \equiv \Gamma_{GeV} - \Gamma_{TeV}$. The location of the cut-off depends on the redshift of the source. The cutoff energy decreases as the redshift increases. (Dwek and Krennrich, 2013).

In the region $\sim$ 1-10 GeV (which is unaffected by EBL absorption), a single power-law can be fitted to a VHE γ-ray source Orr et al. (2011). If we assume that the intrinsic blazar spectra follow this power law to energies $\sim$ 1 TeV, then any spectral break in the observed spectrum can be attributed to EBL absorption. In this method, spectral break analysis, the

knowledge of the intrinsic blazar spectrum is not required to study the EBL Orr et al. (2011). Different studies are used and different assumptions are made for the intrinsic spectra of the γ-ray sources, which leads to the variation of the limits derived by this method.

2.5 A brief discussion of the Fermi-LAT

The Fermi Gamma-Ray Space Telescope was launched into low-earth orbit in the summer of 2008 (Atwood et al., 2009). Since Fermi's launch, its Large Area Telescope (LAT) observes the entire sky in high-energy gamma rays every three hours, creating the most detailed map of the Universe ever known at these energies. The Fermi telescope can measure the diffuse background as well as resolve point sources. It is sensitive to photon energies ranging from 20 MeV up to $\sim$ 100 GeV.

Extragalactic γ-rays and cosmology

The extragalactic γ-ray sky offers a unique opportunity to explore phenomena at cosmological distances. The EBL can be studied indirectly through its effect on very-high energy photons that are emitted by cosmic sources and absorbed via γ γ interactions during their propagation across cosmological distances. This radiation (EBL) is accumulated over the cosmic history, and redshifted by the expansion of the universe Acciari et al. (2019). The Fermi Large Area Telescope (LAT, Atwood et al. (2009)) is a pair conversion detector consisting of a 4x4 array of silicon strip trackers and tungsten converters and a Cesium Iodide (CsI) based calorimeter. The instrument is fully covered by a segmented anti-coincidence shield which provides a highly efficient vetoing against charged particle background events. The LAT is sensitive to gamma rays from 20 MeV to more than 300 GeV. It normally operates in survey mode, covering the whole sky every three hours and providing an instantaneous field of view of 2.4 sr (that is, 20 % of the sky).

Chapter III

Method

3.1 Introduction

In this Chapter I will discuss all the steps followed for the calculation of the EBL from (Bruzual and Charlot, 2003) population synthesis models mentioned in Section 2.1.2. The software package used in this work is discussed in Section 3.2.1. The calculation of the EBL is discussed in Section 3.3.3. The calculation of the Emissivity is discussed in Section 3.4. The absorption and re-emission is discussed in Section 3.4.5, the best-fit model is discussed in Section 3.5 and lastly, the Gamma-ray attenuation is discussed in Section 3.6.

In this work, we use a stellar population synthesis code by (Bruzual and Charlot, 2003) to compute the light produced by stars in galaxies. This code predicts the spectral evolution of stellar populations at wavelengths from 91 Å to 160 μm, at ages between 1x10^5 and 2x10^{10} yr, for different metallicities, initial mass functions (IMFs) and star formation histories. Synthetic galaxy spectral energy distribution (SED) templates are preferred since they can simulate both early and late phases of galaxy evolution (Massarotti et al., 2001). The SEDs of galaxies are created by adding various types of stellar SEDs together. This is done by making a few assumptions about the relationships of different types of stars, the SED models can be designed to match the observed galaxy's SEDs. These assumptions include: (1) the assumption that low metallicity, massive stars dominate young stellar populations of distant galaxies but are relatively rare in the local Universe; (2) Branch (AGB) dominates the integrated light, slight differences in model prescription can lead to substantially different predictions for a population SED, particularly in the near-infrared and (3) the most widely-used stellar population synthesis models make the fundamental assumption that every star evolves independently of any companions, i.e. that all stars are single stars Stanway and Eldridge (2018). The luminosity evolution of stellar populations depends on the amount of interstellar extinction and is sensitive to the IMF (Kneiske et al., 2002). In all applications throughout this thesis, processors involving star formation are based on a Salpeter (1955) IMF.

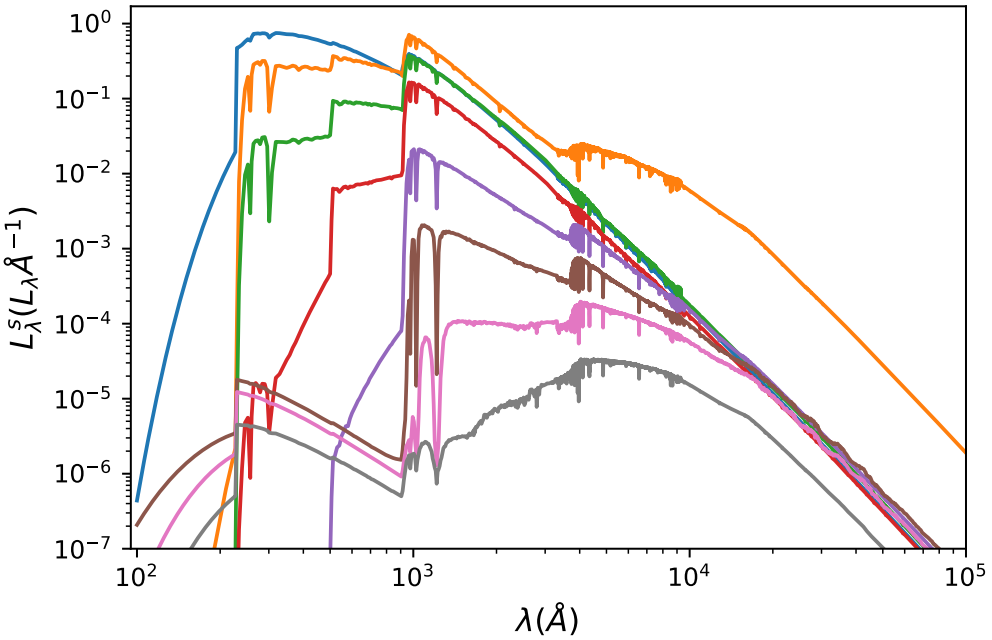


Figure 3.1: SSP spectra for various population ages, for a Salpeter IMF, normalized to 1 $M_\odot$ is depicted in this figure. The spectral energy distribution (SEDs) of a population of coexistent stars, which is expressed as a function of the age of the population. This was calculated for the following ages: $\tau = 0$, 0.0038, 0.00724, 0.0138, 0.07187,0.28612, 1.434, and 11 Gyrs (from top to bottom, based on calculations by (Bruzual and Charlot, 2003). The figure shows a rapid drop in luminosity as massive stars become supernovae (whose light is not included in these SEDs), and the wave- length of the bulk of the emission shifts to the red as the population ages.

The calculation of the evolving spectrum of the EBL discussed in this chapter entails a model of stellar emission and dust attenuation. This model is used to determine the emissivity (luminosity density) corresponding to a star formation history, which is then used to calculate the comoving power spectrum of the EBL. Thereafter, we investigate the effects of varying the star formation rate on the EBL and the γ-ray opacity of the Universe.

3.2 SSP Software Models

3.2.1 GALAXEV

GALAXEV is a software package that is utilised in the computation of the spectral evolution of stellar populations for galaxies. It was released in 2003 by Bruzual and Charlot

(2003). The SEDs are produced in two modes which include two different resolutions: Its low-resolution counterpart wavelength range is from 91 Å to 160 μm with wavelength sampling of 1221 points per spectrum. Both high and low-resolution share a wide range of ages from 1×10^5 to 2×10^{10} yr. The parameters of the simple stellar population (SSPs) include ages, metallicities, the Padova 1994 library (details of this library is discussed in Bruzual and Charlot (2003)) as suggested by Girardi et al. (2000)) evolutionary tracks within the mass range 0.1 to 100 $M_\odot$ for the lower and upper mass cutoff range, m_L = 0.1 $M_\odot$ and m_U = 100 $M_\odot$, respectively. These SSPs are normalized to a total mass of 1 $M_\odot$ in stars at age t = 0. This software uses an updated library of observed stellar SEDs predictions called STELIB complied by (Le Borgne et al., 2003) where fundamental stellar parameters along the HR diagram were maximized. The theoretical isochrones are mapped from the library of observed stellar spectra (i.e for any given properties of stellar populations, any SFH can be expanded in a series of instantaneous starbursts (SSP), and is suitable for population synthesis modelling). The model proposed by Bruzual and Charlot (2003) has been proven to reproduce the observed optical and NIR colour-magnitude diagram (CMD) of Galactic star clusters of various ages and metallicities. Their model has been compared to several observations of star clusters. The spectral fit can constrain physical parameters such as metallicity, SFH and dust content of galaxies. GALAXEV has been tested by (Bruzual and Charlot, 2003), who found that it can reproduce in detail the typical galaxy spectra extracted from the SDSS Early Data Release by Schneider et al. (2002). Furthermore, GALAXEV is one of the first models to enable accurate studies of absorption line features over all ages that reproduce simultaneously the observed strengths of the Lick indices (the Lick index system is a method used to derive the average stellar population characteristics through the evolutionary synthesis of integrated spectra (Fan et al., 2016)) at that epoch (Bruzual and Charlot, 2003). This opens up the possibility of exploring new indices over the full wavelength range from 3200 to 9500 Å. For star-forming galaxies studies, the attenuation of starlight by dust can be included in the modelling Bruzual and Charlot (2003).

3.3 Individual spectra extraction from GALAXEV and its connection to the computation of the EBL

3.3.1 Bruzual & Charlot (2003)

In this work, we used a program called `galaxevpl`, provided by the GALAXEV program, launched by the alias command `gpl`. It reads a binary `*.ised` file as defined in the (Bruzual and Charlot, 2003) documentation which enables the user to access individual spectra (up to 24) at various ages (in Gyrs). Once the spectra are selected, the data are written into a multi-column file that can be plotted. The user can specify a wavelength range and the program will write the spectra into a file, the flux units, and lastly, the name of the output file can be modified according to the user's preference. By default, the spectra are output as luminosity

per unit wavelength. The spectral evolutionary models produced by the Bruzual & Charlot code are stored as binary files. The program also assumes that the files fed into the program are in binary format. A program called `bin_ised` is provided that translates from text to binary format.

3.3.2 Extracting individual spectra

Here is a summary of the procedures followed in the creation of galaxy SEDs from the GALAXEV program:

- The SSPs were converted from ASCII format into binary files using the `bin_ised` program.
- The `galaxevpl` program was used to read the binary files, by extracting one individual spectrum for a given wavelength range and at selected ages in Gyrs (we used an SSP with low metallicity in this work). The selected spectra were written into a multi-column file and saved. By default, the spectral output was in units of luminosity per unit wavelength ($L_{\odot}\text{Å}^{-1}$). The resulting spectra were plotted over the given wavelength range.

3.3.3 Computation of the Extragalactic Background Light (EBL)

The modelling for the absorption and re-emission of the EBL leads to the comprehension of how the production of the EBL affects the opacity observed as a function of redshift. The opacity, which is manifestation of the removal of γ-rays from view, alters observations from extragalactic sources.

A semi-empirical forward evolution (see Section 2.2.2) model is used in the calculation of the stellar part of the EBL in this work. The rest of this chapter will be devoted to explanations of detailed calculations of the EBL.

3.4 Calculation of the Emissivity

The calculation of the luminosity density involves the convolution of the specific luminosity, $L_{\nu}(t)$, the star formation rate density and the Jacobian ($\left|\frac{dt'}{dz'}\right|$), which incorporates the cosmology. To arrive at this point, we need to develop a model that predicts the luminosities of the SEDs as a function of cosmic time, which in this work were constructed from realistic stellar evolution tracks with detailed atmospheric models. A Salpeter IMF between 0.1 and 100 $M_{\odot}$ was used in the construction of these SEDs.

The luminosity density, also known as the emissivity, is given by the following equation:

$$\varepsilon_\nu(z) = \int_z^{z_m} L_\nu(t(z) - t(z'))\dot{\rho}_*(z') \left|\frac{dt'}{dz'}\right| dz' \,, \tag{3.1}$$

where $\dot{\rho}_*(z')$ is the star formation rate per comoving unit volume. The star formation rate is assumed to have begun at a finite epoch $z_m = z(t_m)$. $\left|\frac{dt'}{dz'}\right|$ is the Jacobian. The details and application of the above equation will be discussed in the following sections.

3.4.1 Spectral Synthesis model

A "universal" initial mass function is used to describe how stars convert gas into stars, given by a stellar-mass distribution (Madau and Dickinson, 2014). A simple stellar population SSP refers to several stars produced by a spontaneous explosion that abruptly converts gas into stars (see Section 2.1.1 and Kneiske et al. (2002)). The evolution of the interstellar medium of galaxies is driven by massive stars. Massive stars in the SSP typically produce UV radiation, are short-lived ($\sim 10^7$ yrs) and can ionize surrounding atomic hydrogen gas. This ionized gas is heated by the photo-electrons and cooled through forbidden line radiation of trace species such as oxygen, resulting in a temperature of some 10^4 K (Mokiem et al., 2004). Low-mass stars produce red light and remain within the main sequence (see Section 2.1.2). Stars progress over various cosmological times, depending on their mass. This makes the SEDs of these populations a sensitive function of time (Kneiske et al., 2002).

In this work, we the used Bruzual & Charlot population synthesis model (BC-model) to trace the varying production of energy as a function of time. A depiction of multiple SEDs produced at specific times after the explosion is shown in Figure 3.1. The stellar spectra used in synthesizing the SEDs stem from Padova (Bruzual and Charlot, 2003) and Lejeune stellar atmosphere models (Lejeune et al., 1997). The spectra of elliptical galaxies can be approximated using a single explosion of star formation, which is reassuring since the SEDs fabricated using this code resemble these galaxies.

3.4.2 Low metallicity SEDs

According to the Russell-Vogt theorem, the position of a star on the HR diagram is determined by its mass and composition. The luminosity of a star is mainly determined by its central temperature and composition. As mentioned in Section 3.4.1, the time dependence of the luminosity of stars is set by the time dependence of mass and the rate of change of its composition. This is evident in the nuclear burning regions of a star. However, the chemical composition of stars is important, as lower metallicity stars are less opaque to radiation. The radiation escapes more efficiently in lower metallicity stars than higher metallicity stars; as a

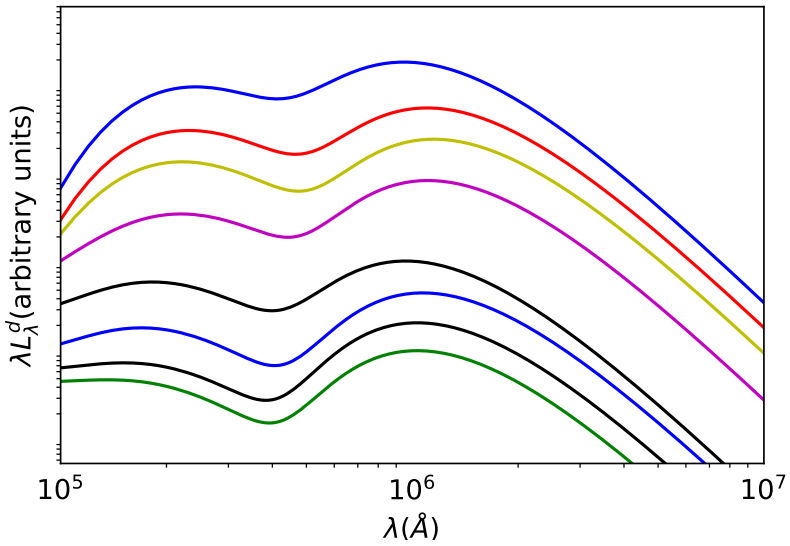


Figure 3.2: This figure depicts the IR spectra associated with each SSP-spectrum (updated Bruzual and Charlot (2003) stellar populations) shown in Figure 3.1. We assume the dust emits as a combination of three blackbodies, representing three types of dust: a 37 K blackbody representing warm, large dust grains, a 80 K blackbody representing hot, small dust grains, and a 202 K blackbody representing PAHs. Thus, the IR emission is modelled as the sum of three modified blackbody spectra. The details of this calculation are mentioned in Section 3.4.5

result of this, these stars tend to be smaller and hotter at the surface for the same luminosity. Smaller stars tend to be hotter in the middle, thus making them more luminous. Overall, the evolution of the luminosity of low metallicity stars is much faster than those of higher metallicity. In this work, we used SEDs of low metallicity. The calculation of the infrared spectra produced in Figure 3.2 involves the calculation of the bolometric luminosity at each age listed in Figure 3.1. A low metallicity star produces a more luminous SEDs, and thus a slightly higher bolometric luminosity. This may account for the slight deviation observed in our plot compared to the IR spectra in Figure 2 of (Kneiske et al., 2002), which was calculated using solar metallicity Z=0.02. In addition, lower metallicity in the stellar atmospheres leads to a higher fraction of light primarily emitted in the UV, and subsequently redistributed towards the IR by interstellar dust grains, with extinction parameters determined newly from the fit to the emissivities (i.e. independent of the assumed low metallicity in the stellar atmospheres producing the bulk of the light Kneiske et al. (2002)). See Figure 6 in Kneiske et al. (2002) for an illustration of the comparison of the low metallicity EBL to the standard model with solar metallicity.

3.4.3 Interstellar medium and dust attenuation

To obtain the correct SEDs, processes such as intrinsic absorption that occur in the galactic interstellar medium (ISM) must be considered. In this work, we assumed a homogeneous dispersion of the gas enclosing the stars of the SSP, which was done for simplicity. We also applied Osterbrock's (Osterbrock, 1989) Case B recombination for optically thick clouds at an equilibrium temperature of 10^4 K, mentioned in detail in Section: 3.4.5.

3.4.4 Average Dust extinction

The average metallicity of gas in galaxies slowly increases with cosmic time; the present value was not known at the time Kneiske et al. (2002) was written. For this reason, the following average extinction curve was adopted:

$$A_\lambda = 0.68 \times E(B-V) \times (\lambda^{-1} - 0.35)\ . \tag{3.2}$$

where A_λ with λ [Å] is the average dust extinction and $R = 3.2$ (the parameter R $\equiv$A(V)$E(B-V)$, the ratio of total to selective extinction at V-band), $E(B-V) = 0.14$ was used for young SSPs and $E(B-V) = 0.03$ was used for older SSPs.

Equation 3.2 was used to calculate the dust extinction curve and was used to determine the absorption coefficient

$$g(\lambda) = 10^{-0.4 \cdot A_\lambda}\ . \tag{3.3}$$

3.4.5 Re-emission computed as the addition of three modified Blackbody spectra

Equation 3.4 is a numerical representation of the modelling used in the calculation of the infrared spectrum. The starlight that is absorbed by dust is reradiated in the infrared. There are generally thought to be three major dust components in the interstellar medium (e.g. Desert et al. (1990)): (1) a large grain component that absorbs optical light and reradiates in the far-IR, found in and around star-forming regions; (2) A small grain component that absorbs the far UV and reradiates in the near-IR, located throughout the disk of spiral galaxies and is responsible for most of the observed dust radiation and (3) a component from polycyclic aromatic hydrocarbons (PAHs) which emit as broad emission lines and are not generally in thermodynamic equilibrium with their environment Dwek et al. (1997). Thus, in this work the IR emission is computed as the modification of three blackbodies, each of which symbolize a specific temperature related to the dust components found in the ISM. These

Table 3.1: Dust parameters used in the calculation of the dust spectra of the EBL.

Dust component	Temperatures	Dust Parameters (c_1, c_2, c_3)
Cold Dust	37 K	10^{-10}
Warm dust	80 K	10^{-24}
PAH molecules	202 K	10^{-20}

components are classified as cold dust, warm dust and polyaromatic hydrocarbons (PAH) for short.

The spectra of the re-emission is calculated as follows (Kneiske et al., 2002):

$$L_{\lambda}^{d}(L_{bol}) = \sum_{i=1} c_i(L_{bol}) Q_{\lambda} B_{\lambda}(T_i) \, . \tag{3.4}$$

where $Q_{\lambda} \propto \lambda^{-1}$ is the extinction efficiency factor, $B_{\lambda}(T_i)$ is the Planck function at temperature T_i ,$L_{bol} = L_{bol}(\tau)$, L_{bol} is the bolometric luminosity and τ represents the age of the stellar population. The dust components found the ISM are characterized as follows, $(c_1, T_1), (c_2, T_2)$ and (c_3, T_3), represents cold dust, warm dust and PAH molecules, at the three temperatures T_i, i = 1...3 and three constants c_i, i = 1...3, respectively. Observations from non-Seyfert galaxy observations by Spinoglio et al. (1995) were used to fix the 6 model parameters in Equation 3.4. The relation was fit for four bands, 12 μm, 25 μm , 60 μm, and 100 μm from Spinoglio et al. (1995) observations. Non-Seyfert galaxy observations were used to normalize the components $c_i, i = 1, 2, 3$ relative to each other.

The Fitting procedure

The $L_{bol} = L_{bol}(\tau)$ is known as the bolometric luminosity and is defined as the total luminosity integrated over all wavelengths (in the optical band in this case).

We selected distinct ages for each SSP, and thus performed this calculation for each age over the wavelength range in the optical band. The temperatures T_i, i = 1,2,3 stated in Equation 3.4 were used in the fit as free parameters. T_3 = 240 K (which is found in the range presented by Kneiske et al. (2002)), T_2 = 80 K (warm dust), T_1 = 30 K (cold dust) were used as starting temperatures. T_1, T_2 , T_3, were allowed to vary between 27-33K, 70 -25 K, 180-400 K, respectively. The fit was done to find the parameters that best fit the infrared luminosities calculated according to Spinoglio et al. (1995) figures. The actual temperatures used for the fit is given in Table 3.1.

The Absorption is calculated using an Osterbrock Case B recombination

The Lyman-alpha line is a particular line in the hydrogen spectrum, going from n=2 to n=1. The Lyman series are all lines for all transitions to level 1. Ly-α emission can be generated via ionizing radiation in a form of ionization and thermal equilibrium (Gould and Weinberg, 1996). In ionization equilibrium, a Ly-α photon is produced since each ionization leads to recombination. Secondly, the radiation originates from the electron being heated by the gas as a result of the kinetic energy of the ionized electron, which occurs in thermal equilibrium (Gould and Weinberg, 1996). Most of the radiation emitted in the second case is in the form of free-bound, free-free emission or collisional excitation which gives rise to line emission (Gould and Weinberg, 1996). In optically thick clouds (at high densities, and temperature $\sim 10^4$ K), the dominant cooling mechanism is line emission. As a result, a huge fraction of deposited thermal energy is released in Ly-α photons.

In this work, we used the assumption that all the hydrogen ionizing photons are absorbed locally in the interstellar medium. This means that 68% of them (hydrogen ionizing photons) are converted to into Ly-α photons, which is the fraction appropriate for case B recombination in a gas (Pei et al., 1999). The total emissivity required for Bremsstrahlung radiation (the stellar part of the emission) is given by the following equation (Rybicki and Lightman, 2008):

$$\epsilon_\nu = 6.8 \times 10^{-38} n_e n_i T^{-\frac{1}{2}} e^{-\frac{h\nu}{kT}} \bar{g}_{ff} \frac{\text{erg}}{\text{s cm}^3\text{Hz}} . \tag{3.5}$$

where Z is the atomic number of the element (in this case, Z represents the atomic number of hydrogen), $\bar{g}_{ff}$ is the average Gaunt factor, n_e and n_i are the number densities of the electrons and ions, respectively. Using the relation $\lambda\epsilon_\lambda = \nu\epsilon_\nu$, we calculate ϵ_λ. The aim at this point was to calculate ϵ_λ, which is referred to as the optical emission of gas heated by absorbed photons. It is evident from Equation 3.5 that obtaining the correct units for ϵ_λ required the multiplication of a volume element in order to arrive at emissivity in terms of wavelength. Therefore, in order to obtain the correct units in Equation 3.5, the following relation was used to calculate the optical emission of gas heated by absorbed photons:

$$\epsilon_\lambda = c \times \frac{\epsilon_\nu}{\lambda^2} \times V .$$

where V is the volume of the cloud.

A uniform distribution of gas and dust surrounding the stars of the SSP was assumed to simplify the calculations. Osterbrook's Case B recombination was applied for optically thick clouds at an equilibrium temperature of 10^4 K, i.e. total absorption of all ionizing photons and reemission of 68 % of the absorbed power in L_α line emission (which is subsequently absorbed by dust). The remaining energy (32 %) is assumed to be reemitted in the optical regime via bremsstrahlung and recombination line/continuum emission.

The total spectra, including absorption and re-emission computed per SSP-spectrum is written as follows:

$$L_\lambda(\tau) = [(L_{\lambda,BC}(\tau) + c_g(\tau) \cdot \epsilon_\lambda)] \cdot g_\lambda + c_d \cdot L^d_\lambda(\tau) \, . \tag{3.6}$$

where the SEDs provided by the BC-Model are given by $L_{\lambda,BC}(\tau)$ at an age τ. The optical emission of gas heated by absorbed photons is represented by $\epsilon_\lambda \propto \exp(-h\nu/kT)$ which is multiplied by the fractional energy $c_g(\tau)$ of 32% that can be accessed by this channel. The absorption coefficient, given by g_λ modifies both spectral components in the optical band. We then added the contribution from the dust re-emission spectra $L^d_\lambda(\tau)$ according to Equation 3.4. The normalization constant c_d was used to normalize the IR-spectra, through the use of the conservation of energy of the photons that were absorbed and re-emitted. The relation $\lambda L_\lambda(\tau) = \nu L_\nu(\tau)$ was used to calculate the emissivity (see Equation 3.1) .

3.4.6 Cosmology

Kneiske et al. (2002) adopted the flat Friedman cosmology with cosmological parameters: Ω_0 = 1 implies that the universe is spatially flat, Ω_λ = 0 (which is referred to as the constant energy density associated with the "vacuum"), and $h = H_0/100$ km s^{-1} Mpc^{-1}, where H_0 is the Hubble constant and h is a dimensionless (current) Hubble parameter, which were used for the EBL model predictions . The calculation of $t(z)$, which is referred to the age of the universe at redshift z proceeds as follows:

The general expression for the time evolution

$$H_0 t(z) = \int_z^\infty \frac{dz}{(1+z)E(z)} \, . \tag{3.7}$$

where

$$E(z)^2 = \Omega_r(1+z)^4 + \Omega(1+z)^3 + \Omega_\Lambda \, . \tag{3.8}$$

$$E(z) = \sqrt{\Omega(1+z)^3} \, . \tag{3.9}$$

Therefore,

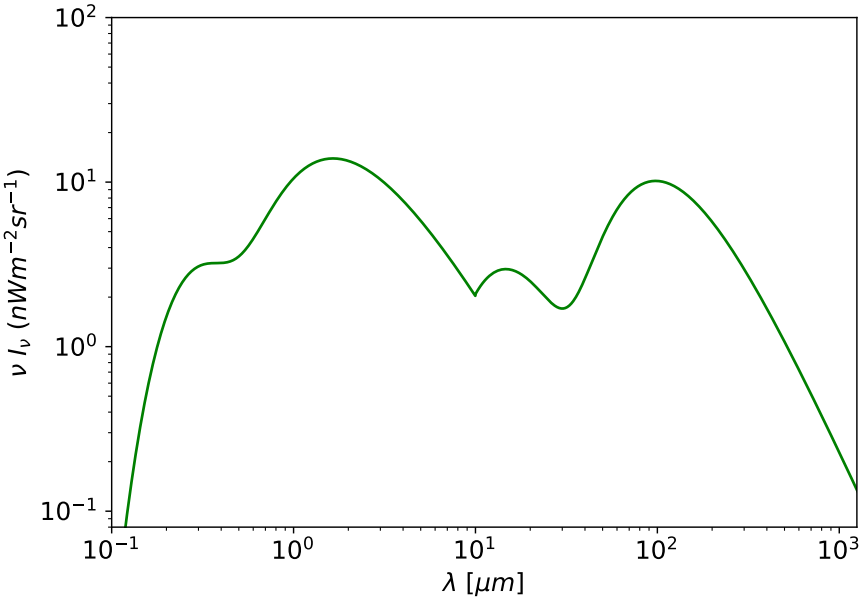


Figure 3.3: This figure depicts the EBL at $z = 0$, calculated using Bruzual and Charlot (2003) stellar population synthesis models at low metallicity ($Z = 0.001$) and best-fit model parameters proposed by Kneiske et al. (2004). The EBL measurements produced in this work agrees with the EBL measurements made by Kneiske et al. (2004) at $z = 0$. These Best-fit model parameters are listed in Table 3.2.

$$t(z) = \frac{1}{H_0} = \int_z^\infty \frac{dz}{(1+z)^{\frac{5}{2}}}\,. \tag{3.10}$$

$$t(z) = \frac{2}{3} H_0^{-1} (1+z)^{-\frac{3}{2}} + C\,. \tag{3.11}$$

The parameters used in Kneiske et al. (2004) were adjusted to Friedman cosmology with the following fixed parameters: Ω_m = 0.3, Ω_Λ= 0.7 and h = 0.75 which corresponds to the cold dark matter cosmology (ΛCDM).

The star formation rate density SFRD(z) and the SEDs calculated from a spontaneous explosion of star formation were used to calculate the emissivity at distinct frequencies and redshifts (Khaire and Srianand, 2015). An assumed IMF along with the metallicity Z, provide SEDs that are functions of age τ and frequency $\nu L_\nu(t)$ in units of erg s^{-1} Hz^{-1} per unit mass of stars formed at different ages, τ, of the stellar population as mentioned in earlier sections. Due to the short timescales at which star formation processes occur ($10^5 - 10^7$ yrs),

the starburst spectra can be interlaced which the global SFRD(z) to compute the luminosity density, also known as the emissivity $\varepsilon_\nu(z)$ (Khaire and Srianand, 2015).

The comoving emissivity at cosmic epoch t can be derived from the population synthesis starburst models

$$\varepsilon_\nu(t) = \int_{t_m}^{t} L_\nu(t-t')\dot{\rho}_*(t') \left|\frac{dt'}{dz'}\right| dt' \,. \tag{3.12}$$

where $\dot{\tilde{\rho}}_*$(t) is the star formation rate per comoving cosmic epoch. The star formation rate is assumed to have begun at some finite epoch $z_m = z(t_m)$. Therefore, equation (3.12) can be rewritten in terms of redshift by solving the following convolution integral where $\dot{\tilde{\rho}}_*$(t) = $\dot{\rho}_*(z)$ is defined as the star formation rate per comoving unit volume:

$$\varepsilon_\nu(z) = \int_{z}^{z_m} L_\nu(t(z)-t(z'))\dot{\rho}_*(z') \left|\frac{dt'}{dz'}\right| dz' \,. \tag{3.13}$$

where $\dot{\rho}_*(z')$ is the star formation rate per comoving unit volume and $(t(z) - t(z'))$ is a representation of the time or rather the age of the population as a function of the redshift at which the spontaneous explosion of star formation occurred at redshift z'. The burst of star formations occurs at all epochs, t, but with the average star formation rates which are equal to the global SFRD(t), which is captured by the product of $L_\nu(t(z) - t(z'))$ and $\dot{\rho}_*(z')$ in the convolution integral (3.24).

The energy density for a given evolution of the emissivity can be calculated by conducting a second integration over redshift. After multiplying the emissivity by $c/4\pi$, we obtain the comoving power spectrum of the EBL, which is given in intensity units:

$$P_\nu(z) = \nu I_\nu(z) = \int_{z}^{z_m} \varepsilon_{\nu'}(z') \left|\frac{dt'}{dz'}\right| dz' \,. \tag{3.14}$$

with $\nu I_\nu(z)$ is in units of nW m^{-2} sr^{-1} and ν' is represented in Equation 3.24 is given by $\nu' = \nu(1+z')(1+z)$. The factor $\left|\frac{dt'}{dz'}\right|$ takes into account the assumed cosmology (e.g., Peebles (1993)), and is given explicitly by

$$\left|\frac{dt'}{dz'}\right| = \frac{1}{H_0(1+z')\sqrt{\Omega_m(1+z')+\Omega_\Lambda}} \,. \tag{3.15}$$

with H_0, Ω_m, Ω_Λ given by the parameters of the Friedmann Model cosmology which corresponds to the ΛCMD. The spectrum of the EBL computed from the Best-fit model is given by Figure 3.3.

The result of this integral yields the entire history of the light emitted from stars in our Universe.

3.5 Calculation of the EBL using different parameters of star formation rate

The global star formation rate (SFR) $\dot{\rho}_*(z)$ consists of two components (Kneiske et al., 2004):

$$\dot{\rho}_*(z) = \dot{\rho}_*^{OPT}(z) + \dot{\rho}_*^{ULIG}(z)\,. \tag{3.16}$$

The first component (optical (OPT)) accounts for the stars which can be optically detected, the other (Ultra-Luminous Infrared Galaxy (ULIG)) coming from stars hidden by dust which can only be seen looking at infrared or submm wavelength. Each of the $SFRs$ can be approximated with a simple broken power law (Kneiske et al., 2004)

$$\dot{\rho}_*(z) \propto (1+z)^{\alpha} \tag{3.17}$$

with $\alpha = \alpha_m$ (α_m and β_m are the conditions for which α is positive or negative, depending on the value of the redshift at the peak, z_{peak}), for $z \leq z_{peak}$ and $\alpha = \beta_m < 0$ for $z > z_{peak}$. Thus, each SFR provides four parameters, α_m, β_m, z_{peak} and $\dot{\rho}_*(z_{peak})$, see Table3.2.

3.5.1 The Best-fit Model

The parameters used in the best-fit model (in terms of SFH) are derived from observations, namely, galaxy number counts in the optical and infrared wavelength range as well as direct measurements of the EBL. When the best-fit model is used in the computation of the EBL, a sharp cut-off is produced at 0.1 μm. This is caused by the absorption of starlight due to the interstellar gas (Kneiske et al., 2004). Table 3.2 provides a mathematical description of the parameters used in this model.

Table 3.2: SFH parameters used in the calculation of the of the star formation rate .The values were obtained from (Kneiske et al., 2004).

Parameter used to constrain the SFH					
Models	Parameters	α	β	z_p	$\dot{\rho}_*(z_{peak})$
Best-Fit	SFR_{OPT}	3.5	-1.2	1.2	0.1
	SFR_{LIG}	4.5	0	1.0	0.1
	$f_{esc} = 0$				
	$c_2 = 10^{-24}$				

where f_{esc} is the fraction of the ionizing photons that escapes from a galaxy, e.g. through superbubbles blown into the ISM by supernovae.

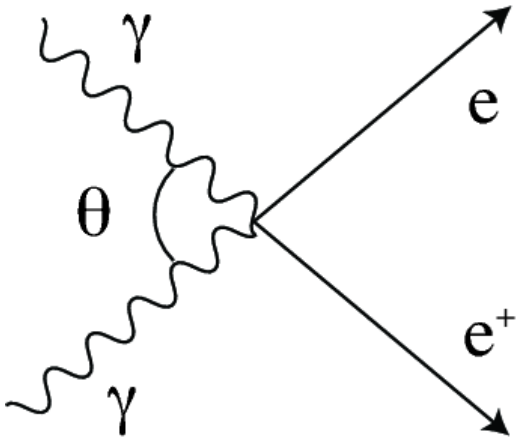


Figure 3.4: This figure illustrates the reaction of the γ-γ pair and depicts the definition of the angle θ between the interacting photons. Figure adopted from (Dwek and Krennrich, 2013)

3.6 Gamma-ray attenuation

A particle and anti-particle pair is created from the interaction between two photons with energies E_γ and ϵ. However, this process only occurs when the total γ-ray energy energy in the center of momentum of the system exceeds the rest frame energy of the two particles.

The threshold energy for the creation of an e^+ + e^- pair is given by Dwek and Krennrich (2013) :

$$\epsilon_{th}(E_\gamma, \mu) = \frac{(2m_e c^2)^2}{E_\gamma(1-\mu)} \,. \tag{3.18}$$

where $\mu \equiv \cos\theta$, and θ is the angle between the two photons (Dwek and Krennrich, 2013, see Figure 3.4).

The cross-section for the γ-γ interaction is given by (Dwek and Krennrich, 2013):

$$\sigma_{\gamma\gamma} = \frac{3}{16}\sigma_T(1-\beta^2)[2\beta(\beta^2-2) + (3-\beta^4)\ln\left(\frac{1+\beta}{1-\beta}\right)] \,. \tag{3.19}$$

where

$$\beta \equiv \sqrt{(1-\frac{\epsilon_{th}}{\epsilon})} \,. \tag{3.20}$$

σ_T is the Thomson cross section.

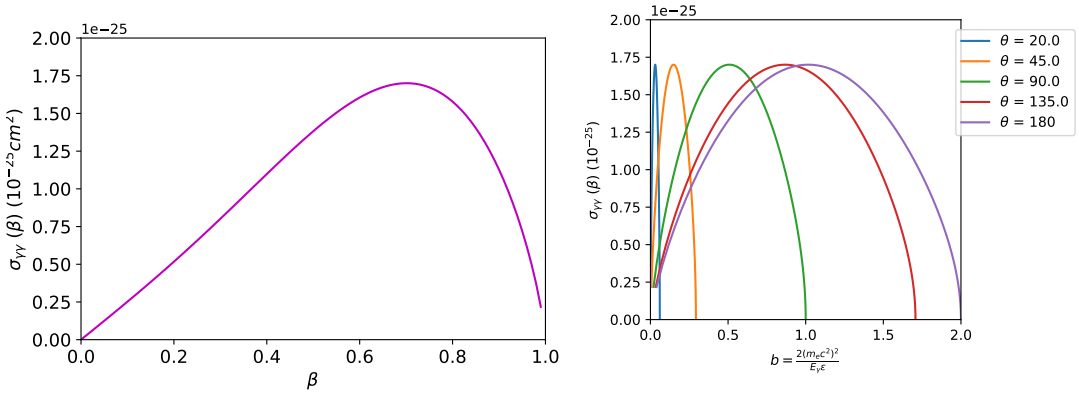


Figure 3.5: The cross section for the γ-γ interaction **Left panel:** The cross section's dependence on β (see Equation 3.19) ; **Right panel:** The cross section's dependence on various incident angles.

The (left panel) of Figure 3.5 depicts the cross section as a function of β. The cross section peaks at a value of β = 0.70, providing a relation between the energies E_γ and ϵ (or wavelength λ) at the peak, given by:

$$E_\gamma = \frac{1.07}{\epsilon(eV)(1-\mu)} = \frac{0.86\lambda(\mu m)}{1-\mu} \tag{3.21}$$

The right panel of the figure depicts the cross section as a function of $b \equiv \frac{(2m_e c^2)^2}{E_\gamma \varepsilon}$ for different values of the angle θ. When the photons are moving in the same direction (θ = 0), the cross section collapses to a delta-function at b = 0, and the energy threshold becomes infinite.

The optical depth for $\gamma - \gamma$ attenuation

The following equation was used for the determination of the optical depth (Dwek and Krennrich, 2013):

$$\tau_{\gamma\gamma}(E_\gamma, z) = \int_0^{z_q} \frac{dl}{dz'} dz' \int_{-1}^{1} d\mu \frac{(1-\mu)}{2} \int_{\epsilon_{min}}^{\infty} d\epsilon \sigma_{\gamma\gamma}(E_\gamma, \epsilon, \mu, z)(1+z')^3 n_\epsilon(\epsilon, z)\,. \tag{3.22}$$

with the cosmological line element $\frac{dl}{dz'} = c\left|\frac{dt}{dz}\right|$, where l is the proper distance, $\mu = \cos\theta$ is the angle between interacting photons, $n_\epsilon(\epsilon, z)$ is the number density of the EBL (cm^{-3}eV^{-1}) of background photons with energy ϵ at redshift z, $(1+z')^3$ is used in the conversion of the

proper number density and $\sigma_{\gamma\gamma}$ is the pair-production cross section (Dwek and Krennrich, 2013). The threshold for pair-production is $\epsilon_{th'} = \frac{(2m_e c^2)^2}{E_\gamma(1-\mu)(1+z)}$; $(1+z)$ is added to account for the increased energy of a γ-ray photon observed at the redshift at which the interaction occurred. Therefore, $\beta' = \sqrt{1 - \frac{\epsilon_{th'}}{\epsilon}}$, in terms of the threshold for creation. The determination of how opaque the EBL is to γ-rays from distant astrophysical sources necessitates knowledge of how the specific number density evolves with redshift $n_\epsilon(\epsilon, z)$. The relationship between the specific EBL intensity and the specific number density of photons with energy ϵ at redshift z is given by (Dwek and Krennrich, 2013):

$$\epsilon^2 n_\epsilon(\epsilon, z) = \frac{4\pi}{c} \nu I_\nu(\nu, z) \, . \tag{3.23}$$

$$n_\epsilon(\epsilon, z) = \frac{4\pi}{c} \frac{1}{\epsilon^2} \nu I_\nu(\nu, z) \tag{3.24}$$

where ϵ is the energy of a photon, given by $\epsilon = h\nu$, $\nu I_\nu(\nu, z)$ is the specific intensity of the EBL given by Equation 3.24 in nW m^{-2} sr^{-1}. Therefore, n_ϵ is in units of cm^{-3}eV^{-1}.

Chapter IV

Results and discussion

4.1 Topics of the investigation

As discussed in section 3.5, we used a best-fit model for the star formation history with parameters listed in Table 3.2. The luminosity density was derived at three different wavelength bands in the optical region, between 0< z < 4. We calculated the comoving EBL at five different redshifts. Lastly, we calculated the opacity at five different redshifts and compared our results to Fermi-LAT observations.

4.1.1 Best fit Star formation rate model and Emissivity

In our model, the stars in galaxies are all represented by SSPs. The emissivity is obtained for a given star formation rate. The emissivity was calculated at three different wavelength bands in the optical region. The star formation results from a burst of star formation that lasts for up to 10^5-10^7 yrs as mentioned in Chapter 3. The stars have low metallicity ($Z = 0.001$) for a Salpeter IMF. We assumed total absorption of ultraviolet starlight due to interstellar gas. As mentioned in Chapter 3, the parameters used in the best fit model interpolate the data from galaxy number counts at optical and infrared wavelengths optimally. In Figure 4.1, the star formation increases between 0 and 1.1 and decreases from 1.1 towards higher redshifts. Upon analysis of the model used in the calculation of the extragalactic background light, we observed a sharp cut-off at $0.1\mu m$ due to the total absorption of UV starlight by interstellar gas.

Emissivity

The emissivity was calculated at three different wavelength bands in the optical region. The best fit model used in this work is similar to the CSFR model used in Kneiske and Mannheim (2000), with the star formation increasing up to a redshift of $z = z_b \sim 1 - 2$ and decreases

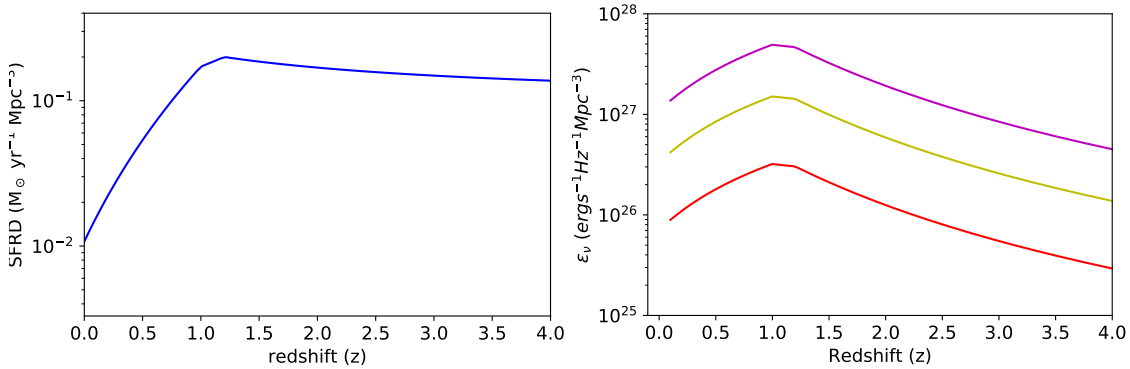


Figure 4.1: This figure illustrates the relationship between the model luminosity density as a function of redshift and a given a star formation rate model. **Left panel:** Total global star formation rate for Kneiske et al. (2004), best-fit model $SFR = SFR_{OPT} + SFR_{LIG}$; **Right panel:** The model emissivities are plotted at 1.0 μm, 0.44 μm, 0.28 μm wavelength bands in the optical region from top to bottom.

at $z > z_b$. Naturally the shape of the UV-luminosity density curve is similar to the that of the SFR. As stars form, they become hotter and brighter. Most of the radiation is emitted in the UV band-optical wavelengths. This accounts for the increase in the luminosity and the wavelength increases. This effect is observed in Figure 3.1: the luminosity drops rapidly as stars become supernovae. As the population ages, a large portion of emission of the wavelengths becomes redder.

In a similar way, a steeper increase at 0.28 μm and the shallower increase at 1.0 μm are well reproduced by our model. However, the emissivity produced by our model is slightly lower than the emissivity produced by Kneiske and Mannheim (2000). This might be due to the fact that the parameters in their work are not exactly the same.

4.1.2 The EBL at various redshifts using best-fit model

At a given redshift, the EBL is the accumulated emission over the history of the Universe, minus the amount lost to absorption, plus the amount re-emitted by dust over time. This changes because stars are continuously formed and die. Figure 4.2 represents the EBL at four different redshifts based on the model proposed by Kneiske et al. (2002). These plots were produced using updated (Bruzual and Charlot, 2003) stellar population synthesis models with metallicity $Z = 0.001$ as the exact SSP used in Kneiske et al. (2004) was not listed. These plots resemble the plots published in Kneiske et al. (2004). The temperatures used for the dust re-emission lie within the range published in Kneiske et al. (2002). The absorption part of the spectrum (Equation 3.6) was challenging to reproduce as the normalization constants

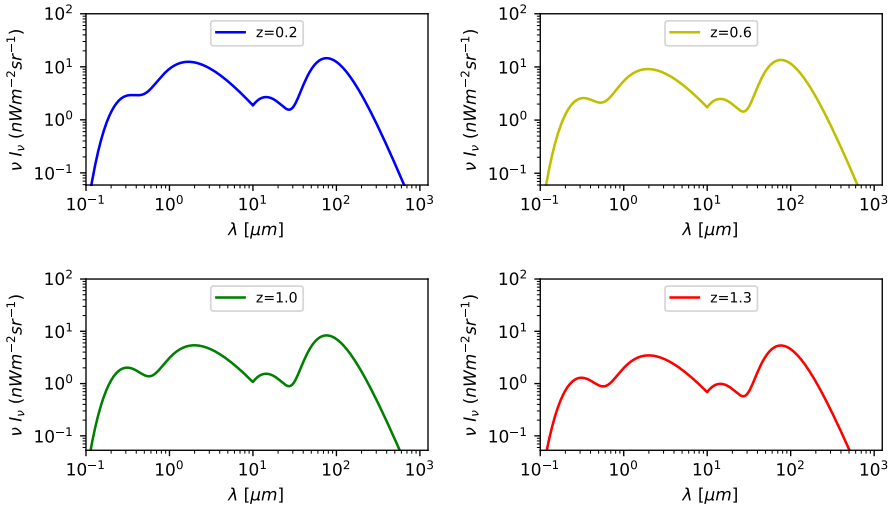


Figure 4.2: The comoving-frame EBL using the best-fit model proposed by Kneiske et al. (2004) with updated (Bruzual and Charlot, 2003) models.

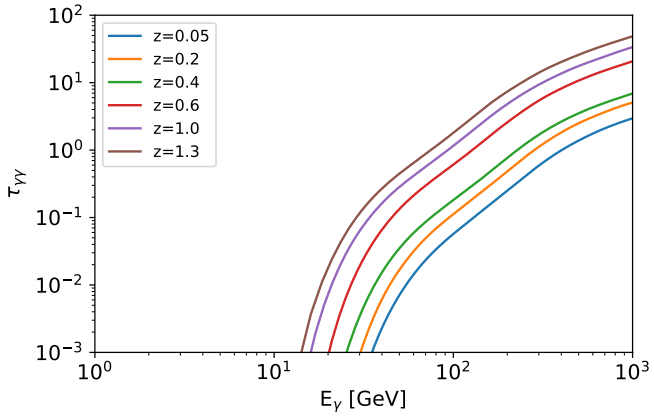


Figure 4.3: This figure illustrates the γ-ray opacity of the Universe at different redshifts, calculated using observed E_γ energies in GeV. The calculations are based on the Kneiske et al. (2004) model.

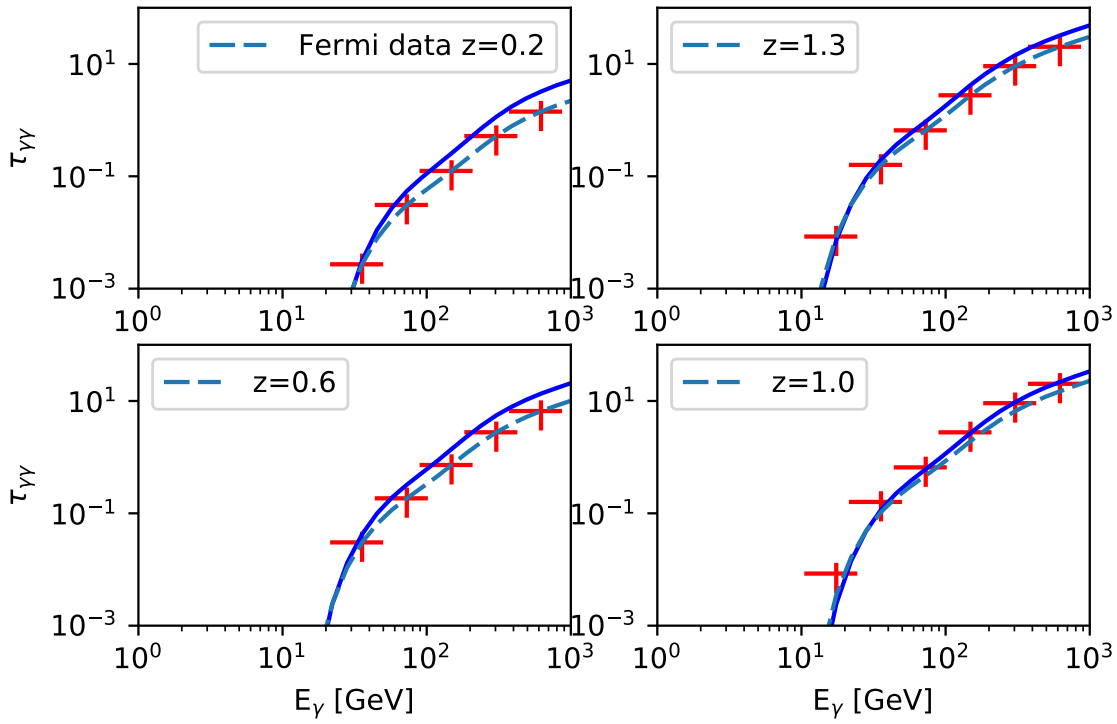


Figure 4.4: This figure illustrates the γ-ray opacity of the Universe at different redshifts, where the dashed lines represent the data from Fermi observations Fermi-LAT Collaboration et al. (2018). The solid line shows the predictions of the Kneiske et al. (2004) EBL model. It is apparent from the figure that most of the constraining power is around $\tau_{\gamma\gamma}$ =1 (Tajima, 2013). The value $\tau_{\gamma\gamma}$ = 1 marks the cosmic γ-ray horizon, i.e., the energy above which our Universe becomes opaque to γ-rays for a given redshift. The Fermi data are depicted with error bars.

used in the model were not provided. According to Equation 3.6 the total emissivity required for Bremsstrahlung requires an electron number density, column density and the radius at which the cloud becomes optically thick, which were also not provided. The values for the electron number density used in this work were $\sim 10^4$ cm^{-3} based on the temperature of $\sim 10^4$ K as listed in Kneiske et al. (2002).

Fermi-LAT Collaboration et al. (2018) analysed γ-ray photons detected by the Large Area Telescope (LAT) instrument on the Fermi γ-ray Space Telescope, over 9 years of operations. The sample used in this analysis consists of 739 blazars, galaxies hosting a super-massive black hole with a relativistic jet pointed at a small angle to the line of sight. See section 2.4 and 2.5 for more details.

At any epoch, the EBL is composed of the emission of all stars that existed up to that point in time and can therefore be used to infer properties related to the evolution of galaxy populations. In this work, we use the parameters for the SFH from Kneiske et al. (2004) to calculate the EBL, which was then used to calculate the optical depth.

Fermi-LAT Collaboration et al. (2018) calculated the cosmic SFH using two independent approaches: 1) by using a reconstructed UV emissivity across cosmic time to derive the SFH from established relations between the UV luminosity and star-formation rate. 2) by using a physical EBL model to calculate the optical depth due to the EBL directly from the SFH. The SFH was then optimized using a Markov Chain Monte Carlo (MCMC) to reproduce the Fermi-LAT optical depth data. According to the latter, the opacity is supposed to provide a constraint on the SFH. Thus, in this work the Fermi data was used to constrain the parameters of the SFH developed by Kneiske et al. (2004).

According to Fermi-LAT Collaboration et al. (2018), the Fermi-LAT dataset is tightly constraining at UV, optical and, at low redshifts, also near-IR wavelengths) and should provide the tightest constraints around redshift, 0.5-1.5 as the opacity increases for larger distances travelled, shown in Figure 4.4. In addition to this, the confidence regions grow larger towards mid-IR wavelengths due to the energy range of Fermi LAT being limited to < 1 TeV. Figure 4.4 depicts how the computed EBL fits to the Fermi data. The solid line shows the predictions of the Kneiske et al. (2004) EBL model and the red error bars represent the Fermi data. Based on the analysis of Figure 4.4, it is evident that the results obtained from the updated EBL model is closer to the Fermi data than Kneiske et al. (2004). This means that our updated model, which uses the Best-fit model for the SFH developed by Kneiske et al. (2004) and updated stellar populations Bruzual and Charlot (2003) with low metallicity are validated by the improved agreement with the Fermi data.

4.1.3 Summary of different models used to calculate the EBL, including the model used in this work

In Malkan and Stecker (1998), IR luminosity functions from IRAS were extrapolated backwards in redshift using power-law functions. The model of Stecker et al. (2006) updated this work and computed the EBL below the Lyman limit (13.6 eV) for two different cases of stellar evolution. The model of Rowan-Robinson (2001) also utilized a 60 μ m evolving luminosity function, and a four-component spectral model for IR and optical emission. One potential problem with this method was that it had difficulty accounting for the emissivity contribution of merger-triggered starbursts, believed to have contributed an increasing fraction of the SFR density and IR emissivity with increasing redshift. Franceschini et al. (2001) tried to account for this starburst phase in a backwards evolution model. Franceschini et al. (2008) published a sophisticated model using observed luminosity functions, and used it to calculate the EBL and γ-ray attenuation. This model used evolving luminosity functions in the near-IR up to z = 1.4 for two different galaxy populations (spiral and spheroidal) and local luminosity functions for the irregular/starbursting population, combined with synthetic SEDs to find the total emissivity. The infrared component of Franceschini et al. (2008) model is comparable to that of the best-fit model of Kneiske et al. (2004), and similarly, it over predicts the 250 μm BLAST (Marsden et al., 2009) measurement and the Cosmic Background Explorer (COBE) (Fixsen et al., 1998) infrared data.

Kneiske et al. (2002) calculated the EBL from the UV to far-IR using a 'semi-empirical' method based on measured star formation rates and spectral synthesis models. Light is reprocessed by dust and gas; dust is modelled as a blackbody with 3 temperature components. Metallicity is assumed to increase slowly over cosmic time and an average global extinction curve is applied to starlight. A follow-up paper, Kneiske et al. (2004) (model used in this thesis), expanded this earlier model into 6 realizations, varying in gas temperature contribution, star formation rate, and UV escape fraction. The result from the Kneiske et al. (2002, 2004) papers are based upon a broken power-law for the star-formation history, with a peak at z = 1.2.

Stecker et al. (2006) have used a backward-evolution model based on observations of the infrared luminosity function to calculate the IR EBL energy density. They then used a forward-evolution model similar to Salamon and Stecker (1998) to calculate the optical/UV EBL, and normalize it to their backward-evolution calculation.

Gilmore et al. (2009) presented models based on semianalytic models of galaxy evolution, using cosmological parameters from Wilkinson Microwave Anisotropy Probe (WMAP) and normalizing their semi-analytic model's luminosity density prediction to local luminosity density measurements. They also included a component from quasars and realistically

treated extinction of ionizing radiation by the intergalactic medium, both of which had implications for the UV portion of the EBL at high redshift. Gilmore et al. (2009) only treated the UV–optical portion of the EBL. The 'best-fit' EBL in Kneiske et al. (2004) is considerably higher than Gilmore et al. (2009) fiducial model in both the optical and far-IR peaks.

Razzaque et al. (2009), presented EBL models in the optical through ultraviolet by consistently considering the star formation rate (SFR), initial mass function (IMF), and dust extinction, and treating stars on the main sequence as blackbodies. Finke et al. (2010) (which was an extension of Razzaque et al. (2009)'s model) presented an inferred evolution model for the UV through IR components of the EBL from the direct stellar radiation and reprocessed stellar radiation by the dust. This model considered the star formation rate, initial mass function, dust extinction and main-sequence stars as black bodies. The model is also extended to include the post-main sequence stars and reprocessing of starlight by the dust. The total energy absorbed by the dust is assumed to be re-emitted as three blackbodies in the IR, one at 40 K (warm, large dust grains), one at 70 K (hot, small dust grains) and one at 450 K (polycyclic aromatic hydrocarbons). This model does not require a complex stellar structure code or semi-analytical models of the galaxy formation. The work presented in Finke et al. (2010) is significantly below the models of Kneiske et al. (2004) and Stecker et al. (2006) for all wavelengths.

An update to this work by Kneiske and Dole (2010) attempted to create a model using a similar method that produceed a minimal background, and a similar method was employed in Razzaque et al. (2009), Finke et al. (2010).

Gilmore et al. (2012) presented a new semi-analytic model that is based on galaxy formation in a Five-year Wilkinson Microwave Anisotropy Probe (WMAP5) cosmology, which has already been discussed in Section 2.2.4.

4.1.4 Gamma-ray opacity of the Universe

When EBL photons interact with propagating GeV/TeV gamma-ray photons, opacity is created due to the production of electron-positron pairs. The determination of the opacity of the Universe to γ-rays is important for several VHE γ-ray observations such as the Fermi γ-ray Space telescope and High Energy Stereoscopic System (H.E.S.S). Figure 4.3 gives an illustration of the gamma-ray optical depth based on Equation 3.30. The optical depth was calculated for observed energies (E_γ), and several redshifts in the energy range from 0.1 eV to 10 eV. The observed energy range was from 1-1000 GeV. Higher opacity would be expected at higher energies and higher redshifts, and lower opacity at lower energies and lower redshifts, consistent with the figure, since the EBL is transparent to at low energy γ rays.

Chapter V

Conclusions

The spectrum of the extragalactic background light is of fundamental importance in galaxy evolution and γ-ray astronomy. As a new feature, we reproduced the Kneiske et al. (2002) model, using updated (Bruzual and Charlot, 2003) low metallicity (Z= 0.001) stellar population synthesis models as well as the best-fit SFRD model proposed by Kneiske et al. (2004). The EBL produced in this work resembles the work published in Kneiske et al. (2004). As mentioned in Chapter 4, the deviation may be due to various factors, namely the normalization factor used in the absorption model (radius, electron number density and column density) as well as the exact SSP used in the analysis.

According to Equation 3.4, the re-emission spectrum depends on the bolometric luminosity. This means that if the luminosity of the SSPs increase, the bolometric luminosity increases as well increased dust re-emission spectrum. In (Kneiske et al., 2002),the EBL was computed using solar metallicity with lower dust re-emission. The dust spectrum in Kneiske et al. (2004) is higher than the absorption spectrum in Paper II (Kneiske et al. (2004)). This is evident in our work as well.

The results obtained in Figure 4.4 provide evidence of a strong correlation between the updated EBL model and the Fermi data. This means that our updated model, which uses the Best-fit model for the SFH developed by Kneiske et al. (2004) and updated stellar populations Bruzual and Charlot (2003) with low metallicity are validated by the improved agreement with the Fermi data.

In addition to this, I expected to see higher opacity at higher energies and higher redshifts, and lower opacity at lower energies and lower redshifts, which is consistent with the figure. The opacity produced in this work appears to match the observations found by Fermi-LAT, (for the given redshifts used in our work) but deviate slightly at redshifts 0.2, 0.6, 1.0 and 1.3. The results produced in this work are in agreement with the literature.

Bibliography

V. A. Acciari, S. Ansoldi, L. A. Antonelli, A. Arbet Engels, D. Baack, Babić, A. , B. Banerjee, U. Barres de Almeida, J. A. Barrio, J. Becerra González, W. Bednarek, L. Bellizzi, E. Bernardini, A. Berti, J. Besenrieder, W. Bhattacharyya, C. Bigongiari, A. Biland, O. Blanch, G. Bonnoli, G. Busetto, R. Carosi, G. Ceribella, Y. Chai, S. Cikota, S. M. Colak, U. Colin, E. Colombo, J. L. Contreras, J. Cortina, S. Covino, V. D'Elia, P. Da Vela, F. Dazzi, A. De Angelis, B. De Lotto, M. Delfino, J. Delgado, F. Di Pierro, E. Do Souto Espiñeira, A. Domínguez, D. Dominis Prester, D. Dorner, M. Doro, D. Elsaesser, V. Fallah Ramazani, A. Fattorini, A. Fernández-Barral, G. Ferrara, D. Fidalgo, L. Foffano, M. V. Fonseca, L. Font, C. Fruck, D. Galindo, S. Gallozzi, R. J. García López, M. Garczarczyk, S. Gasparyan, M. Gaug, Godinović, N. , D. Green, D. Guberman, D. Hadasch, A. Hahn, T. Hassan, J. Herrera, J. Hoang, D. Hrupec, S. Inoue, K. Ishio, Y. Iwamura, H. Kubo, J. Kushida, A. Lamastra, D. Lelas, F. Leone, E. Lindfors, S. Lombardi, F. Longo, M. López, R. López-Coto, A. López-Oramas, B. Machado de Oliveira Fraga, C. Maggio, P. Majumdar, M. Makariev, M. Mallamaci, G. Maneva, M. Manganaro, K. Mannheim, L. Maraschi, M. Mariotti, M. Martínez, S. Masuda, D. Mazin, Mić, anović, S. , D. Miceli, M. Minev, J. M. Miranda, R. Mirzoyan, E. Molina, A. Moralejo, D. Morcuende, V. Moreno, E. Moretti, P. Munar-Adrover, V. Neustroev, A. Niedzwiecki, M. Nievas Rosillo, C. Nigro, K. Nilsson, D. Ninci, K. Nishijima, K. Noda, L. Nogués, M. Nöthe, S. Paiano, J. Palacio, M. Palatiello, D. Paneque, R. Paoletti, J. M. Paredes, P. Peñil, M. Peresano, M. Persic, P. G. Prada Moroni, E. Prandini, I. Puljak, W. Rhode, M. Ribó, J. Rico, C. Righi, A. Rugliancich, L. Saha, N. Sahakyan, T. Saito, K. Satalecka, T. Schweizer, J. Sitarek, Šnidarić, I. , D. Sobczynska, A. Somero, A. Stamerra, D. Strom, M. Strzys, Surić, T. , F. Tavecchio, P. Temnikov, Terzić, T. , M. Teshima, N. Torres-Albà, S. Tsujimoto, J. van Scherpenberg, G. Vanzo, M. Vázquez Acosta, I. Vovk, M. Will, Zarić, and D. . Measurement of the extragalactic background light using MAGIC and Fermi-LAT gamma-ray observations of blazars up to z = 1. *MNRAS*, 486(3):4233–4251, July 2019. doi: 10.1093/mnras/stz943.

M. Ackermann, M. Ajello, and Allafort. The Imprint of the Extragalactic Background Light in the Gamma-Ray Spectra of Blazars. *Science*, 338(6111):1190, Nov 2012. doi: 10.1126/science.1227160.

W. B. Atwood, A. A. Abdo, M. Ackermann, W. Althouse, B. Anderson, M. Axelsson, L. Baldini, J. Ballet, D. L. Band, G. Barbiellini, J. Bartelt, D. Bastieri, B. M. Baughman, K. Bechtol, D. Bédérède, F. Bellardi, R. Bellazzini, B. Berenji, G. F. Bignami, D. Bisello, E. Bissaldi, R. D. Blandford, E. D. Bloom, J. R. Bogart, E. Bonamente, J. Bonnell, A. W. Borgland , A. Bouvier, J. Bregeon, A. Brez, M. Brigida, P. Bruel, T. H. Burnett, G. Busetto, G. A. Caliandro, R. A. Cameron, P. A. Caraveo, S. Carius, P. Carlson, J. M. Casandjian, E. Cavazzuti, M. Ceccanti, C. Cecchi, E. Charles, A. Chekhtman, C. C. Cheung, J. Chiang, R. Chipaux, A. N. Cillis, S. Ciprini, R. Claus, J. Cohen-Tanugi, S. Condamoor, J. Conrad, R. Corbet, L. Corucci, L. Costamante, S. Cutini, D. S. Davis, D. Decotigny, M. DeKlotz, C. D. Dermer, A. de Angelis, S. W. Digel, E. do Couto e Silva, P. S. Drell, R. Dubois, D. Dumora, Y. Edmonds, D. Fabiani, C. Farnier, C. Favuzzi, D. L. Flath, P. Fleury, W. B. Focke, S. Funk, P. Fusco, F. Gargano, D. Gasparrini, N. Gehrels, F. X. Gentit, S. Germani, B. Giebels, N. Giglietto, P. Giommi, F. Giordano, T. Glanzman, G. Godfrey, I. A. Grenier, M. H. Grondin, J. E. Grove, L. Guillemot, S. Guiriec, G. Haller, A. K. Harding, P. A. Hart, E. Hays, S. E. Healey, M. Hirayama, L. Hjalmarsdotter, R. Horn, R. E. Hughes, G. Jóhannesson, G. Johansson, A. S. Johnson, R. P. Johnson, T. J. Johnson, W. N. Johnson, T. Kamae, H. Katagiri, J. Kataoka, A. Kavelaars, N. Kawai, H. Kelly, M. Kerr, W. Klamra, J. Knödlseder, M. L. Kocian, N. Komin, F. Kuehn, M. Kuss, D. Landriu, L. Latronico, B. Lee, S. H. Lee, M. Lemoine-Goumard, A. M. Lionetto, F. Longo, F. Loparco, B. Lott, M. N. Lovellette, P. Lubrano, G. M. Madejski, A. Makeev, B. Marangelli, M. M. Massai, M. N. Mazziotta, J. E. McEnery, N. Menon, C. Meurer, P. F. Michelson, M. Minuti, N. Mirizzi, W. Mitthumsiri, T. Mizuno, A. A. Moiseev, C. Monte, M. E. Monzani, E. Moretti, A. Morselli, I. V. Moskalenko, S. Murgia, T. Nakamori, S. Nishino, P. L. Nolan, J. P. Norris, E. Nuss, M. Ohno, T. Ohsugi, N. Omodei, E. Orlando, J. F. Ormes, A. Paccagnella, D. Paneque, J. H. Panetta, D. Parent, M. Pearce, M. Pepe, A. Perazzo, M. Pesce-Rollins, P. Picozza, L. Pieri, M. Pinchera, F. Piron, T. A. Porter, L. Poupard, S. Rainò, R. Rando, E. Rapposelli, M. Razzano, A. Reimer, O. Reimer, T. Reposeur, L. C. Reyes, S. Ritz, L. S. Rochester, A. Y. Rodriguez, R. W. Romani, M. Roth, J. J. Russell, F. Ryde, S. Sabatini, H. F. W. Sadrozinski, D. Sanchez, A. Sand er, L. Sapozhnikov, P. M. S. Parkinson, J. D. Scargle, T. L. Schalk, G. Scolieri, C. Sgrò, G. H. Share, M. Shaw, T. Shimokawabe, C. Shrader, A. Sierpowska-Bartosik, E. J. Siskind, D. A. Smith, P. D. Smith, G. Spandre, P. Spinelli, J. L. Starck, T. E. Stephens, M. S. Strickman, A. W. Strong, D. J. Suson, H. Tajima, H. Takahashi, T. Takahashi, T. Tanaka, A. Tenze, S. Tether, J. B. Thayer, J. G. Thayer, D. J. Thompson, L. Tibaldo, O. Tibolla, D. F. Torres, G. Tosti, A. Tramacere, M. Turri, T. L. Usher, N. Vilchez, V. Vitale, P. Wang, K. Watters, B. L. Winer, K. S. Wood, T. Ylinen, and M. Ziegler. The Large Area Telescope on the Fermi Gamma-Ray Space Telescope Mission. *ApJ*, 697(2):1071–1102, June 2009. doi: 10.1088/0004-637X/697/2/1071.

N. Bavouzet, H. Dole, E. Le Floc'h, K. I. Caputi, G. Lagache, and C. S. Kochanek. Esti-

mating the total infrared luminosity of galaxies up to $z \sim 2$ from mid- and far-infrared observations. *A&A*, 479(1):83–96, Feb 2008. doi: 10.1051/0004-6361:20077896.

R. Blandford, D. Meier, and A. Readhead. Relativistic Jets from Active Galactic Nuclei. *ARA&A*, 57:467–509, Aug 2019. doi: 10.1146/annurev-astro-081817-051948.

M. Boquien, D. Burgarella, Y. Roehlly, V. Buat, L. Ciesla, D. Corre, A. K. Inoue, and H. Salas. CIGALE: a python Code Investigating GALaxy Emission. *A&A*, 622:A103, Feb 2019. doi: 10.1051/0004-6361/201834156.

V. Bosch-Ramon. Gamma rays from extragalactic astrophysical sources. In M. R. Zapatero Osorio, J. Gorgas, J. Maíz Apellániz, J. R. Pardo, and A. Gil de Paz, editors, *Highlights of Spanish Astrophysics VI*, pages 97–106, Nov 2011.

D. Branch. Supernovae. 2003.

G. Bruzual and S. Charlot. Stellar population synthesis at the resolution of 2003. *MNRAS*, 344(4):1000–1028, Oct 2003. doi: 10.1046/j.1365-8711.2003.06897.x.

M. Burton. *Radiation*, 2017 (accessed August 20, 2020). `https://www.britannica.com/science/radiation`.

D. Calzetti and T. M. Heckman. The Evolution of Dust Opacity in Galaxies. *ApJ*, 519(1): 27–47, July 1999. doi: 10.1086/307338.

B. Carroll and D. Ostlie. *An Introduction to Modern Galactic Astrophysics and Cosmology*. Pearson Addison Education, 2006. ISBN 9780805303476. URL `https://books.google.co.za/books?id=9VKiAAAACAAJ`.

F. Chris. *Free-Free or Bremsstrahlung Scattering*, 2001 (accessed August 24, 2020). `http://www.astro.utu.fi/~cflynn/Stars/l6.html`.

S. Cole, A. Aragon-Salamanca, C. S. Frenk, J. F. Navarro, and S. E. Zepf. A recipe for galaxy formation. *MNRAS*, 271:781–806, Dec 1994. doi: 10.1093/mnras/271.4.781.

S. Cole, P. Norberg, C. M. Baugh, C. S. Frenk, J. Bland-Hawthorn, T. Bridges, R. Cannon, M. Colless, C. Collins, W. Couch, N. Cross, G. Dalton, R. De Propris, S. P. Driver, G. Efstathiou, R. S. Ellis, K. Glazebrook, C. Jackson, O. Lahav, I. Lewis, S. Lumsden, S. Maddox, D. Madgwick, J. A. Peacock, B. A. Peterson, W. Sutherland, and K. Taylor. The 2dF galaxy redshift survey: near-infrared galaxy luminosity functions. *MNRAS*, 326 (1):255–273, Sep 2001. doi: 10.1046/j.1365-8711.2001.04591.x.

L. Costamante. Gamma-Rays from Blazars and the Extragalactic Background Light. *International Journal of Modern Physics D*, 22(13):1330025-83, Aug 2013. doi: 10.1142/S0218271813300255.

J. I. Davies, S. Phillipps, M. Trewhella, and P. Alton. Luminosity evolution, extragalactic background light and the opacity of the Universe. *MNRAS*, 291(1):59–64, Oct 1997. doi: 10.1093/mnras/291.1.59.

F.-X. Desert, F. Boulanger, and J. Puget. Interstellar dust models for extinction and emission. *Astronomy and Astrophysics*, 237:215–236, 1990.

R. Diehl. *Gamma-Ray Production with Absorption Processes*, pages 9–26. 2001.

A. Domínguez, J. D. Finke, F. Prada, J. R. Primack, F. S. Kitaura, B. Siana, and D. Paneque. Detection of the Cosmic γ-Ray Horizon from Multiwavelength Observations of Blazars. *ApJ*, 770(1):77, Jun 2013. doi: 10.1088/0004-637X/770/1/77.

L. Dunne, S. Eales, M. Edmunds, R. Ivison, P. Alexander, and D. L. Clements. The SCUBA Local Universe Galaxy Survey - I. First measurements of the submillimetre luminosity and dust mass functions. *MNRAS*, 315(1):115–139, June 2000. doi: 10.1046/j.1365-8711.2000.03386.x.

E. Dwek. The Evolution of the Elemental Abundances in the Gas and Dust Phases of the Galaxy. *ApJ*, 501:643, Jul 1998. doi: 10.1086/305829.

E. Dwek. The evolution of the elemental abundances in the gas and dust phases of the galaxy. *The Astrophysical Journal*, 501(2):643–665, jul 1998. doi: 10.1086/305829. URL `https://doi.org/10.1086%2F305829`.

E. Dwek. The role of dust in producing the cosmic infrared background. *Symposium - International Astronomical Union*, 204:389–400, 2001. doi: 10.1017/S0074180900226314.

E. Dwek and F. Krennrich. The extragalactic background light and the gamma-ray opacity of the universe. *Astroparticle Physics*, 43:112–133, Mar 2013. doi: 10.1016/j.astropartphys.2012.09.003.

E. Dwek, R. Arendt, D. Fixsen, T. Sodroski, N. Odegard, J. Weiland, W. Reach, M. Hauser, T. Kelsall, S. Moseley, et al. Detection and characterization of cold interstellar dust and polycyclic aromatic hydrocarbon emission, from cobe observations. *The Astrophysical Journal*, 475(2):565, 1997.

C. Ertley. Studying the polarization of hard x-ray solar flares with the gamma ray polarimeter experiment (grape). In *American Astronomical Society Meeting Abstracts# 223*, volume 223, 2014.

C. Ertley, P. Bloser, T. Connor, J. Legere, M. L. McConnell, and J. M. Ryan. Measuring the Polarization of Hard X-Ray Solar Flares with GRAPE. In *AGU Fall Meeting Abstracts*, volume 2012, pages SH43B–2173, Dec. 2012.

S. M. Fall and Y. Pei. Cosmic chemical evolution. In *Bulletin of the American Astronomical Society*, volume 31, page 923, 1999.

Z. Fan, R. de Grijs, B. Chen, L. Jiang, F. Bian, and Z. Li. Lick Indices and Spectral Energy Distribution Analysis Based on an M31 Star Cluster Sample: Comparisons of Methods and Models. *AJ*, 152(6):208, Dec 2016. doi: 10.3847/0004-6256/152/6/208.

Fermi-LAT Collaboration, S. Abdollahi, M. Ackermann, M. Ajello, W. B. Atwood, L. Baldini, J. Ballet, G. Barbiellini, D. Bastieri, J. Becerra Gonzalez, R. Bellazzini, E. Bissaldi, R. D. Blandford, E. D. Bloom, R. Bonino, E. Bottacini, S. Buson, J. Bregeon, P. Bruel, R. Buehler, R. A. Cameron, R. Caputo, P. A. Caraveo, E. Cavazzuti, E. Charles, S. Chen, C. C. Cheung, G. Chiaro, S. Ciprini, J. Cohen-Tanugi, L. R. Cominsky, J. Conrad, D. Costantin, S. Cutini, F. D'Ammando, F. de Palma, A. Desai, S. W. Digel, N. Di Lalla, M. Di Mauro, L. Di Venere, A. Domínguez, C. Favuzzi, S. J. Fegan, J. Finke, A. Franckowiak, Y. Fukazawa, S. Funk, P. Fusco, G. Gallardo Romero, F. Gargano, D. Gasparrini, N. Giglietto, F. Giordano, M. Giroletti, D. Green, I. A. Grenier, L. Guillemot, S. Guiriec, D. H. Hartmann, E. Hays, K. Helgason, D. Horan, G. Jóhannesson, D. Kocevski, M. Kuss, S. Larsson, L. Latronico, J. Li, F. Longo, F. Loparco, B. Lott, M. N. Lovellette, P. Lubrano, G. M. Madejski, J. D. Magill, S. Maldera, A. Manfreda, L. Marcotulli, M. N. Mazziotta, J. E. McEnery, M. Meyer, P. F. Michelson, T. Mizuno, M. E. Monzani, A. Morselli, I. V. Moskalenko, M. Negro, E. Nuss, R. Ojha, N. Omodei, M. Orienti, E. Orlando, J. F. Ormes, M. Palatiello, V. S. Paliya, D. Paneque, J. S. Perkins, M. Persic, M. Pesce-Rollins, V. Petrosian, F. Piron, T. A. Porter, J. R. Primack, G. Principe, S. Rainò, R. Rand o, M. Razzano, S. Razzaque, A. Reimer, O. Reimer, P. M. Saz Parkinson, C. Sgrò, E. J. Siskind, G. Spandre, P. Spinelli, D. J. Suson, H. Tajima, M. Takahashi, J. B. Thayer, L. Tibaldo, D. F. Torres, E. Torresi, G. Tosti, A. Tramacere, E. Troja, J. Valverde, G. Vianello, M. Vogel, K. Wood, and G. Zaharijas. A gamma-ray determination of the Universe's star formation history. *Science*, 362(6418):1031–1034, Nov 2018. doi: 10.1126/science.aat8123.

J. D. Finke, S. Razzaque, and C. D. Dermer. Modeling the Extragalactic Background Light from Stars and Dust. *ApJ*, 712(1):238–249, Mar 2010. doi: 10.1088/0004-637X/712/1/238.

M. Fioc and B. Rocca-Volmerange. PEGASE: a UV to NIR spectral evolution model of galaxies. Application to the calibration of bright galaxy counts. *A&A*, 500:507–519, Oct 1997.

D. Fixsen, E. Dwek, J. C. Mather, C. Bennett, and R. Shafer. The spectrum of the extragalactic far-infrared background from the cobe* firas observations. *The Astrophysical Journal*, 508(1):123, 1998.

A. Franceschini, P. Mazzei, G. de Zotti, and L. Danese. Luminosity Evolution and Dust Effects in Distant Galaxies: Implications for the Observability of the Early Evolutionary Phases. *ApJ*, 427:140, May 1994. doi: 10.1086/174127.

A. Franceschini, H. Aussel, C. Cesarsky, D. Elbaz, and D. Fadda. A long-wavelength view on galaxy evolution from deep surveys by the infrared space observatory. *Astronomy & Astrophysics*, 378(1):1–29, 2001.

A. Franceschini, H. Aussel, C. J. Cesarsky, D. Elbaz, and D. Fadda. A long-wavelength view on galaxy evolution from deep surveys by the Infrared Space Observatory. *A&A*, 378:1–29, Oct 2001. doi: 10.1051/0004-6361:20011175.

A. Franceschini, G. Rodighiero, and M. Vaccari. Extragalactic optical-infrared background radiation, its time evolution and the cosmic photon-photon opacity. *A&A*, 487(3):837–852, Sep 2008. doi: 10.1051/0004-6361:200809691.

A. Franceschini, G. Rodighiero, and M. Vaccari. Extragalactic optical-infrared background radiation, its time evolution and the cosmic photon-photon opacity. *Astronomy & Astrophysics*, 487(3):837–852, 2008.

R. C. Gilmore, P. Madau, J. R. Primack, R. S. Somerville, and F. Haardt. Gev gamma-ray attenuation and the high-redshift uv background. *Monthly Notices of the Royal Astronomical Society*, 399(4):1694–1708, 2009.

R. C. Gilmore, R. S. Somerville, J. R. Primack, and A. Domínguez. Semi-analytic modelling of the extragalactic background light and consequences for extragalactic gamma-ray spectra. *MNRAS*, 422(4):3189–3207, June 2012. doi: 10.1111/j.1365-2966.2012.20841.x.

L. Girardi, A. Bressan, G. Bertelli, and C. Chiosi. Evolutionary tracks and isochrones for low-and intermediate-mass stars: From 0.15 to 7, and from to 0.03. *Astronomy and Astrophysics Supplement Series*, 141(3):371–383, 2000.

K. D. Gordon, K. A. Misselt, A. N. Witt, and G. C. Clayton. The DIRTY Model. I. Monte Carlo Radiative Transfer through Dust. *ApJ*, 551(1):269–276, Apr 2001. doi: 10.1086/320082.

A. Gould and D. H. Weinberg. Imaging the Forest of Lyman Limit Systems. *ApJ*, 468:462, Sept. 1996. doi: 10.1086/177707.

M. G. Hauser and E. Dwek. The Cosmic Infrared Background: Measurements and Implications. *ARA&A*, 39:249–307, Jan. 2001. doi: 10.1146/annurev.astro.39.1.249.

R. Hollow. Ideas for effectively teaching vce astronomy & astrophysics. 2003.

J. D. Jackson. Classical electrodynamics, 1999.

A. Kashlinsky. Cosmic infrared background and early galaxy evolution [review article]. *PhR*, 409(6):361–438, Apr 2005. doi: 10.1016/j.physrep.2004.12.005.

J. Kennicutt, Robert C. The Star Formation Law in Galactic Disks. *ApJ*, 344:685, Sept. 1989. doi: 10.1086/167834.

V. Khaire and R. Srianand. Star Formation History, Dust Attenuation, and Extragalactic Background Light. *ApJ*, 805(1):33, May 2015. doi: 10.1088/0004-637X/805/1/33.

T. M. Kneiske and H. Dole. A lower-limit flux for the extragalactic background light. *A&A*, 515:A19, June 2010. doi: 10.1051/0004-6361/200912000.

T. M. Kneiske and K. Mannheim. Cosmic Star Formation Rate from Gamma-Ray Attenuation. In F. Favata, A. Kaas, and A. Wilson, editors, *Star Formation from the Small to the Large Scale*, volume 445 of *ESA Special Publication*, page 437, June 2000.

T. M. Kneiske, K. Mannheim, and D. H. Hartmann. Implications of cosmological gamma-ray absorption. I. Evolution of the metagalactic radiation field. *A&A*, 386:1–11, Apr 2002. doi: 10.1051/0004-6361:20020211.

T. M. Kneiske, T. Bretz, K. Mannheim, and D. H. Hartmann. Implications of cosmological gamma-ray absorption. II. Modification of gamma-ray spectra. *A&A*, 413:807–815, Jan 2004. doi: 10.1051/0004-6361:20031542.

P. Kroupa. The Initial Mass Function of Stars: Evidence for Uniformity in Variable Systems. *Science*, 295(5552):82–91, Jan 2002. doi: 10.1126/science.1067524.

R. B. Larson and V. Bromm. The First Stars in the Universe. *Scientific American*, 285(6): 64–71, Dec. 2001. doi: 10.1038/scientificamerican1201-64.

J. F. Le Borgne, G. Bruzual, R. Pello, A. Lancon, B. Rocca-Volmerange, B. Sanahuja, D. Schaerer, C. Soubiran, and R. Vilchez-Gomez. VizieR Online Data Catalog: STELIB: A library of stellar spectra at R~2000 (Le Borgne+, 2003). *VizieR Online Data Catalog*, art. III/232, Apr 2003.

C. Leitherer, D. Schaerer, J. D. Goldader, R. M. G. Delgado, C. Robert, D. F. Kune, D. F. de Mello, D. Devost, and T. M. Heckman. Starburst99: Synthesis Models for Galaxies with Active Star Formation. *ApJS*, 123(1):3–40, Jul 1999. doi: 10.1086/313233.

T. Lejeune, F. Cuisinier, and R. Buser. Standard stellar library for evolutionary synthesis. I. Calibration of theoretical spectra. *A&AS*, 125:229–246, Oct 1997. doi: 10.1051/aas:1997373.

P. Madau and M. Dickinson. Cosmic Star-Formation History. *ARA&A*, 52:415–486, Aug 2014. doi: 10.1146/annurev-astro-081811-125615.

P. Madau, L. Pozzetti, and M. Dickinson. The Star Formation History of Field Galaxies. *ApJ*, 498(1):106–116, May 1998. doi: 10.1086/305523.

M. Malkan and F. Stecker. An empirically based calculation of the extragalactic infrared background. *The Astrophysical Journal*, 496(1):13, 1998.

G. Marsden, P. A. Ade, J. J. Bock, E. L. Chapin, M. J. Devlin, S. R. Dicker, M. Griffin, J. O. Gundersen, M. Halpern, P. C. Hargrave, et al. Blast: resolving the cosmic submillimeter background. *The Astrophysical Journal*, 707(2):1729, 2009.

M. Massarotti, A. Iovino, and A. Buzzoni. A critical appraisal of the SED fitting method to estimate photometric redshifts. *A&A*, 368:74–85, Mar 2001. doi: 10.1051/0004-6361:20000553.

K. Mattila and P. Väisänen. Extragalactic background light: inventory of light throughout the cosmic history. *Contemporary Physics*, 60(1):23–44, Jan 2019. doi: 10.1080/00107514.2019.1586130.

M. R. Mokiem, N. L. Martín-Hernández, A. Lenorzer, A. de Koter, and A. G. G. M. Tielens. Metallicity and the spectral energy distribution and spectral types of dwarf O-stars. *A&A*, 419:319–334, May 2004. doi: 10.1051/0004-6361:20040074.

A. Neronov and D. Semikoz. Galactic diffuse gamma-ray emission at tev energy. *Astronomy & Astrophysics*, 633:A94, 2020.

M. Orr, F. Krennrich, and E. Dwek. Strong new constraints on the extragalactic background light in the near-to mid-infrared. *The Astrophysical Journal*, 733(2):77, 2011.

M. R. Orr, F. Krennrich, and E. Dwek. Strong New Constraints on the Extragalactic Background Light in the Near- to Mid-infrared. *ApJ*, 733(2):77, Jun 2011. doi: 10.1088/0004-637X/733/2/77.

D. E. Osterbrock. *Astrophysics of gaseous nebulae and active galactic nuclei*. University Science Books, 1989.

P. J. E. Peebles. *Principles of physical cosmology*. Princeton university press, 1993.

Y. C. Pei, S. M. Fall, and M. G. Hauser. Cosmic Histories of Stars, Gas, Heavy Elements, and Dust in Galaxies. *ApJ*, 522(2):604–626, Sept. 1999. doi: 10.1086/307674.

E. Pueschel. The Extragalactic Background Light: Constraints from TeV Blazar Observations. In *35th International Cosmic Ray Conference (ICRC2017)*, volume 301 of *International Cosmic Ray Conference*, page 1107, Jan 2017.

S. Razzaque, C. D. Dermer, and J. D. Finke. The Stellar Contribution to the Extragalactic Background Light and Absorption of High-Energy Gamma Rays. *ApJ*, 697(1):483–492, May 2009. doi: 10.1088/0004-637X/697/1/483.

M. Rowan-Robinson. The star formation history of the universe: an infrared perspective. *The Astrophysical Journal*, 549(2):745, 2001.

M. A. Ruderman and P. G. Sutherland. Theory of pulsars: polar gaps, sparks, and coherent microwave radiation. *ApJ*, 196:51–72, Feb 1975. doi: 10.1086/153393.

G. B. Rybicki and A. P. Lightman. *Radiative processes in astrophysics*. John Wiley & Sons, 2008.

M. Salamon and F. Stecker. Absorption of high-energy gamma rays by interactions with extragalactic starlight photons at high redshifts and the high-energy gamma-ray background. *The Astrophysical Journal*, 493(2):547, 1998.

E. E. Salpeter. The luminosity function and stellar evolution. *The Astrophysical Journal*, 121:161, 1955.

D. P. Schneider, G. T. Richards, X. Fan, P. B. Hall, M. A. Strauss, D. E. Vand en Berk, J. E. Gunn, H. J. Newberg, T. A. Reichard, C. Stoughton, W. Voges, B. Yanny, S. F. Anderson, J. Annis, N. A. Bahcall, A. Bauer, M. Bernardi, M. R. Blanton, W. N. Boroski, J. Brinkmann, J. W. Briggs, R. Brunner, S. Burles, L. Carey, F. J. Castander, A. J. Connolly, I. Csabai, M. Doi, S. Friedman, J. A. Frieman, M. Fukugita, T. M. Heckman, G. S. Hennessy, R. B. Hindsley, D. W. Hogg, Ž. Ivezić, S. Kent, G. R. Knapp, P. Z. Kunzst, D. Q. Lamb, R. F. Leger, D. C. Long, J. Loveday, R. H. Lupton, B. Margon, A. Meiksin, A. Merelli, J. A. Munn, M. Newcomb, R. C. Nichol, R. Owen, J. R. Pier, A. Pope, C. M. Rockosi, D. H. Saxe, D. Schlegel, W. A. Siegmund, S. Smee, Y. Snir, M. SubbaRao, A. S. Szalay, A. R. Thakar, A. Uomoto, P. Waddell, and D. G. York. The Sloan Digital Sky Survey Quasar Catalog. I. Early Data Release. *AJ*, 123(2):567–577, Feb 2002. doi: 10.1086/338434.

V. Schönfelder. *The Universe in Gamma Rays*. Springer Science & Business Media, 2001.

L. Silva, G. L. Granato, A. Bressan, and L. Danese. Modeling the Effects of Dust on Galactic Spectral Energy Distributions from the Ultraviolet to the Millimeter Band. *ApJ*, 509(1): 103–117, Dec 1998. doi: 10.1086/306476.

L. Spinoglio, M. A. Malkan, B. Rush, L. Carrasco, and E. Recillas-Cruz. Multiwavelength Energy Distributions and Bolometric Luminosities of the 12 Micron Galaxy Sample. *ApJ*, 453:616, Nov 1995. doi: 10.1086/176425.

E. R. Stanway and J. J. Eldridge. Re-evaluating old stellar populations. *MNRAS*, 479(1): 75–93, Sept. 2018. doi: 10.1093/mnras/sty1353.

F. W. Stecker, M. A. Malkan, and S. Scully. Intergalactic photon spectra from the far-ir to the uv lyman limit for 0< z< 6 and the optical depth of the universe to high-energy gamma rays. *The Astrophysical Journal*, 648(2):774, 2006.

F. W. Stecker, M. A. Malkan, and S. T. Scully. Intergalactic Photon Spectra from the Far-IR to the UV Lyman Limit for 0 < z < 6 and the Optical Depth of the Universe to High-Energy Gamma Rays. *ApJ*, 648(2):774–783, Sep 2006. doi: 10.1086/506188.

H. Tajima. Solar-terrestrial environment laboratory, nagoya university, nagoya, aichi, 464-8601, japan e-mail: tajima@ stelab. nagoya-u. ac. jp. In *Quest for the Origin of Particles and the Universe: Proceedings of the KMI Inauguration Conference*, page 206. World Scientific, 2013.

D. J. Thompson. Space detectors for gamma rays (100 MeV-100 GeV): From EGRET to Fermi LAT. *Comptes Rendus Physique*, 16(6-7):600–609, Aug. 2015. doi: 10.1016/j.crhy.2015.07.002.

S. University. *Positron*, May 2014 (accessed March, 2020). `https://astronomy.swin.edu.au/cosmos/P/Positron`.

Q. Yuan, H.-L. Huang, X.-J. Bi, and H.-H. Zhang. Fitting the Extragalactic Background with TeV Gamma Ray Spectra of Blazars. In *International Cosmic Ray Conference*, volume 33 of *International Cosmic Ray Conference*, page 3179, Jan. 2013.